Fuzzy logic based active vibration control using novel photostrictive composites

Singh, Diwakar; Sharma, Saurav; Kumar, Rajeev; Chauhan, Vishal S.; Vaish, Rahul

DOI
10.1016/j.compstruct.2023.116919

Publication date
2023

Document Version
Final published version

Published in
Composite Structures

Composite Structures 313 (2023) 116919

Contents lists available at ScienceDirect

Composite Structures

journal homepage: www.elsevier.com/locate/compstruct

Fuzzy logic based active vibration control using novel photostrictive composites

Diwakar Singh [a,*], Saurav Sharma [b], Rajeev Kumar [a], Vishal S. Chauhan [a], Rahul Vaish [a]

[a] School of Engineering, Indian Institute of Technology Mandi, Mandi 175075, Himachal Pradesh, India
[b] Faculty of Mechanical, Maritime and Materials Engineering, Delft University of Technology, Mekelweg 2, 2628 CD Delft, The Netherlands

ARTICLE INFO

Keywords:
Photostriction
Finite element method
Fuzzy logic control
Composite
Actuator

ABSTRACT

Although conventional actuators like piezoelectric and electrostrictive are efficient, but they required hard wiring, which contaminates the control signal and adds to the weight of the structure. The current study presents a wireless control strategy using photostrictive actuators. Owing to the fortunate combination of photovoltaic effect and converse piezoelectric effect, a photostrictive actuator can generate mechanical strain, when irradiated with light intensity. Limited choices of photostrictive material with high electromechanical coupling coefficient give the motivation to design photostrictive composites. The finite element-based formulation incorporating fuzzy logic controller is employed to study the active vibration control response of cantilever structure when equipped with photostrictive composite actuator. A parametric study has been carried out to study the influence of inclusion's volume fraction on wireless active vibration control of the structure. Control merits have been defined to compare the control performance of different composites. It is found that particulate composites are the better choice for lightweight structure and fiber composites are better if there is no weight constraint.

1. Introduction

Structural vibration control implementing traditional actuators and sensors (i.e., piezoelectric, electrostrictive, magnetostrictive [1–5] has been extensively studied by research fraternity in the last two decades. Such a structure with bonded sensors and actuators with an integrated control unit is known as a smart structure. These conventional intelligent materials (i.e., piezoelectric, electrostrictive, magnetostrictive) have the shortcomings such as electromagnetic noise and extra weight contributed by the circuitry, which is required for energy supply. The advent of photostrictive material i.e., lead lanthanum zirconate titanate (PLZT) doped with WO_3, which is capable of producing strain when irradiated with ultraviolet light [6], revolutionized actuator-based research. A photostrictive actuator can be used to attain less weight, more compact and wirelessly controlled structure.

The photostriction in PLZT arises due to the fortunate coupling of the photovoltaic effect and converse piezoelectric effect. Due to the photovoltaic effect, the irradiated light illumination induces an electric field, which in turn generates mechanical strain (i.e., converse piezoelectric effect). Therefore, photostriction can also be defined as, light-induced, non-thermal dimension change of material. As only a few ceramic materials (such as ZnO [7], $BiFeO_3$ [8], $LiNbO_3$ [9]) can interact with the light spectrum to exhibit photostriction. Most of these photostrictive materials (except $BiFeO_3$) have low electromechanical coupling coefficients, which is not sufficient to attain the actuation required for practical application. The interaction of ceramic material with the light spectrum is limited by their wide band gap. Researchers striving for better photostriction attempted to reduce the energy band gap of ceramic materials by doping. Doping of KN, $0.96(K_{0.48}Na_{0.52})NbO_3$-$0.04(Bi_{0.5}Na_{0.5})O_{3-\delta}$ KNBNZ, and $(Na_{0.5}Bi_{0.5})TiO_3$-$BaTiO_3$ (NBT-BT) with Ni^{+2} ions leads to the development of $KNbO_3$ (KN), $(K_{0.9}Ba_{0.1})(Nb_{0.95}Ni_{0.05})O_{3-\delta}$ (KBNNO) [10], $0.96(K_{0.48}Na_{0.52})NbO_3$-$0.04(Bi_{0.5}Na_{0.5})(Zr_{0.55}Ni_{0.45})O_{3-\delta}$ (KNBNZNO) [11], $(Na_{0.5}Bi_{0.5})TiO_3$-$Ba(Ti_{0.5}Ni_{0.5})O_{3-\delta}$ (NBT-BTNO) [12]. This doping method was successful in creating photostrictive material but its not able to solve the challenge of low electromechanical coupling coefficient.

Due to the simultaneous involvement of thermal, electrical, optical, and mechanical stimuli, photostriction becomes a multiphysics problem incorporating optical, thermal, elastic, piezoelectric, and pyroelectric phenomena. Constitutive modeling equations for photostrictive actuators were developed by Tzou and Chou [13]. Later Liu and Tzou [14] also carried out a study of the photostrictive behavior of PLZT

* Corresponding author.
E-mail address: d19002@students.iitmandi.ac.in (D. Singh).

https://doi.org/10.1016/j.compstruct.2023.116919
Received 15 September 2022; Received in revised form 11 January 2023; Accepted 10 March 2023
Available online 21 March 2023

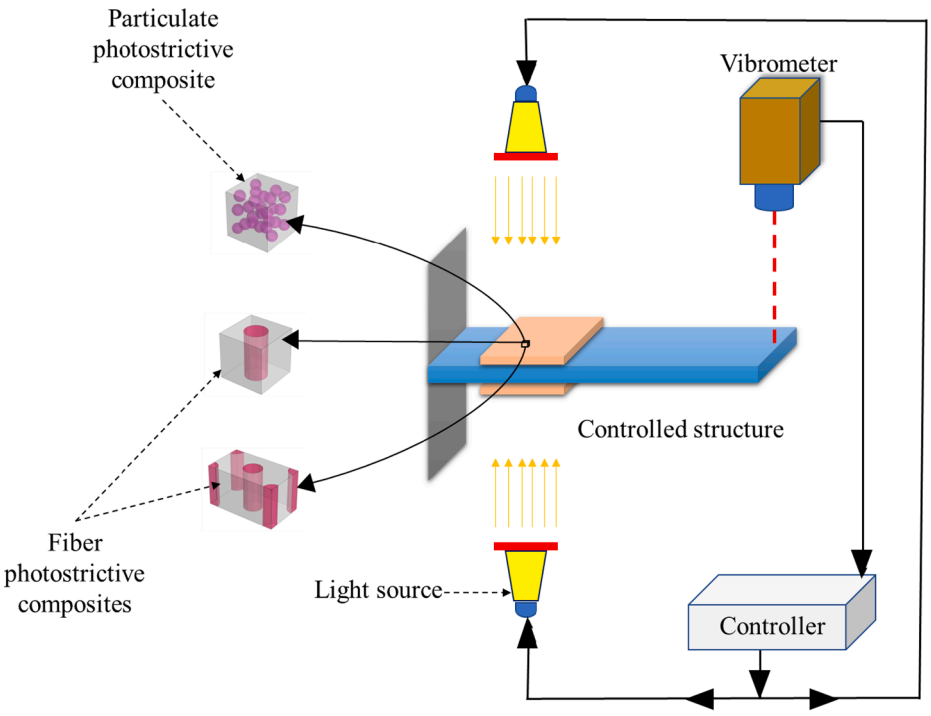

Fig. 1. Schematic of elimination of undesired vibrations from uncontrolled structure using photostrictive composite actuators.

considering photodeformation, pyroelectricity, and thermoelectricity. They also put forward a varying light intensity control of simply supported plate bonded with PLZT. In varying light control, light intensity is proportional to the velocity and its direction depends on the direction of velocity. Model control equations were derived by Shih et al. [15] for an open cylinder shell, while investigating the effect of PLZT actuator's position. Shih et al. [16] also put forward a theoretical model for vibration control of simply supported plate by manipulating the actuator positions. Along with the effect of uniform irradiation and intermittent irradiation of light, similarities and differences between the velocity feedback control and Lyapunov were explored by Wang et al. [17]. Jiang et al. [18] investigated a hybrid model i.e., the vibration control of a simply supported cylindrical shell using both photostrictive (PLZT) and piezoelectric (PVDF) actuators. Sun and Tong [19] also conducted a study on wireless vibration control of structure using PLZT actuator. In the aforementioned research two kinds to control methods were used: Lyapunov (i.e., constant light intensity irradiation) and velocity feedback control (i.e., varying light intensity irradiation). He and Zheng [20,21] implemented fuzzy logic controller for wireless controlling of thin plates and cylindrical shells. These works concluded that a fuzzy logic controller is remarkably better than velocity feedback control [22–24]. He et al. [25,26] also controlled the multi modes of cylindrical shell employing neuro-fuzzy logic controller. Jia et al. [27] applied fuzzy logic controller for vibration suppression of beam considering the non-linear actuating behavior of PLZT. In the aforementioned literature survey of wireless vibration control using photostrictive actuator, most of the researchers have used PLZT as actuator. The reason behind this choice is not only the high electromechanical coupling coefficient of PLZT but also the lack of choices available.

The limitation of choices can be eliminated by designing a photostrictive composite having a large electrotechnical coupling coefficient and able to interact with a wider light spectrum. Such composite can be designed by considering photovoltaic polymer as a matrix and piezoelectric ceramic as particle inclusions or fiber inclusions [28,29]. This solution will help to design the photostrictive composite with desired properties such as low stiffness, high electromechanical coupling coefficient, and can interact with visible light. Present work considers the poly{4,8-bis[5-(2-ethyl-hexyl) thiophen-2-yl]benzo[1,2-b:4,5-b'] dithiophene-2,6-diyl-alt-3-fluoro-2-[(2-ethylhexyl)carbonyl]thieno [3,4-b]thiophene-4,6-diyl} (PTB7-Th) as photovoltaic polymer matrix and $Pb(Mg_{1/3}Nb_{2/3})O_3$-0.35$PbTiO_3$ (PMN-35PT) as piezoelectric inclusion material for the novel photostrictive composites.

A composite's overall behavior can be defined by predicting its effective properties. For the current multiphysics problem researchers have given analytical [30], semi-analytical [31], and mean field models [32]. The aforementioned models were not able to predict all the effective properties, and these were limited to simple shape inclusions. To consider the complex shape inclusions researchers adopted the finite element method for homogenization [28,29]. Berger et al. [33] employed a micromechanical approach to determine the effective elastic and piezoelectric properties of a representative volume element (RVE). The RVE is selected such that it can be periodically repeated in three dimensions to obtain the original composite. A dynamic analysis using the finite element method was put forward [34] to determine particle composite's effective pyroelectric coefficient. Present work designs the novel photostrictive particulate and fiber composite as an alternative to PLZT. The current work firstly evaluates all the multiphysics effective properties of both particulate and fiber composite by varying the volume fraction of inclusions from 6 % to 30 % and 60 % respectively. Secondly to compare the response of designed composites, the vibration control analysis of cantilever structure is carried out by employing velocity feedback and fuzzy logic controllers.

The layout of the current paper is such that modeling, constitutive equations, and numerical homogenization of photostrictive composites are discussed in Section 2. While Section 3 deals with the multiphysics finite element formulation of the laminated structure. Section 4 gives the details of control algorithms, i.e., velocity feedback and fuzzy logic control. Section 5 shows the validation of the current formulation and discusses the various results obtained. At last, all the conclusions drawn from the present study are given in Section 6.

2. Materials and method

The light induced strain enables photostrictive materials to

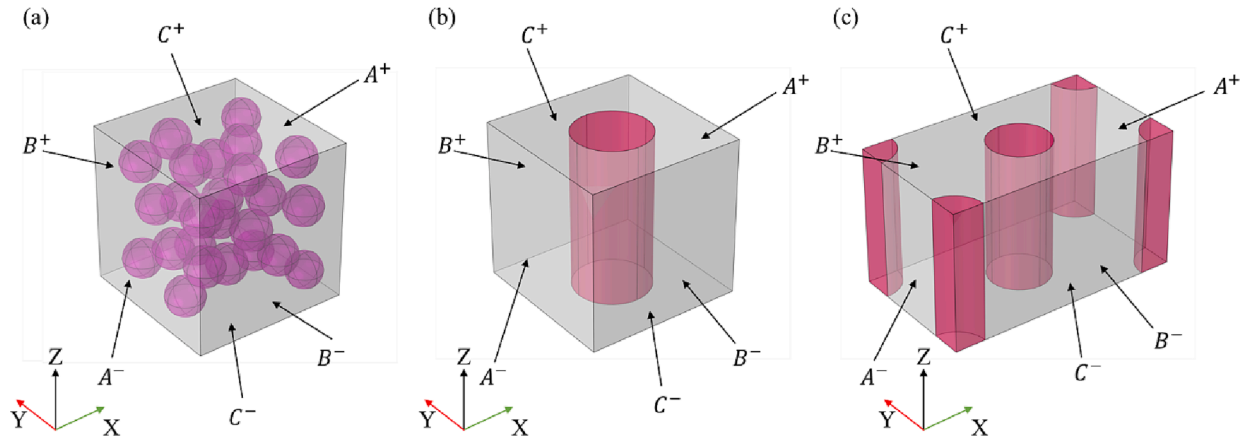

Fig. 2. Representative volume element (RVE) of (a) particulate, fiber composite when fibers aligned in (b) square array, and (c) hexagonal array.

wirelessly eliminate uncontrolled vibration of structures. As shown in Fig. 1, the host structure is bonded with photostrictive actuators on both the upper and lower surfaces. Two actuators are required – on the top and bottom surfaces of the beam – to achieve positive and negative defelction, as light intensity can never be negative. The optical vibrometer can be used to sense the displacement and velocity of the structure at a reference point. We design particulate and fiber photostrictive composites, to be used as actuators in a vibration control application, as shown in Fig. 1. This proposed technical solution i.e. photostrictive composite enhances the possibility of achieving desired qualities, for example, electromechanical coefficient, stiffness, density, and the portion of light spectrum it should interact with.

2.1. Photostrictive actuator

When photostrictive material is irradiated with high-intensity light, charges start flowing in the direction opposite to polarization. In the present study, the actuators are considered to be polarized along the thickness direction. The flow of charges will induce an electrical potential difference between the electrode due to the photovoltaic effect. The induced electric potential difference will lead to mechanical strain owing to the converse piezoelectric effect. While the light is irradiated over the actuator its temperature also increases, this change in actuator's temperature will generate additional electric potential difference due to the pyroelectric effect. Therefore, the total electric field E between the electrodes is [35],

$$E(t) = E_l(t) + E_\theta(t), \tag{1}$$

where t refers to time, E_θ refers to an electric field generated due to the pyroelectric effect. Electrical field E_l induced due to irradiation of light can be calculated as,

$$E_l(t) = E_l\left(t_{j-1}\right) + \left[E_s - E_l\left(t_{j-1}\right)\right]\frac{\alpha^{'}}{a_s} I\left(t_j\right) e^{-\frac{\alpha^{'}}{a_s} I\left(t_j\right)\Delta t}.\Delta t - E_l\left(t_{j-1}\right)\beta e^{-\beta\Delta t}.\Delta t, \tag{2}$$

where E_s is the saturated electric field, $\alpha^{'}$ is the optical-electromechanical actuator constant, a_s is the aspect ratio (i.e., length/width), I is the light intensity, and β is the voltage leakage constant of the photostrictive actuator. The variation of temperature due to irradiation of light can be evaluated as [36],

$$\theta\left(t_{j+1}\right) = \theta\left(t_j\right) + \Delta\theta = \theta\left(t_j\right) + \frac{1}{\rho_m c_m V_m}\left(\alpha A_m I - \frac{\theta_t - \theta_o}{r_m + r_a}\right), \tag{3}$$

where ρ_m is the density, c_m is the specific heat capacity, V_m is the volume, A_m is the surface area of the actuator, θ_o refers to the ambient temperature, which is considered 25 °C. r_m and r_a represents the material thermal and air convective resistances respectively, these terms can be determined as,

$$r_m = \frac{l_m}{k_m A_m}, r_a = \frac{1}{h_a A_m}, \tag{4}$$

where l_m refers to the length of an actuator, k_m is the thermal conductive coefficient, and h_a is the convective heat transfer coefficient. Electric field E_θ induced due to pyroelectric effect is,

$$E_\theta(t) = \frac{p}{b}\theta(t), \tag{5}$$

where p is the pyroelectric coefficient and b is the dielectric constant of the photostrictive actuator. The current based model can be applied to an actuator to determine its pyroelectric coefficient as [34],

$$p = \frac{I_p}{A_m \cdot \frac{d\theta}{dt}} \tag{6}$$

where I_p is the pyroelectric current. The total electrical potential difference $\varnothing_Z$ generated between the electrodes of the photostrictive actuator is,

$$\varnothing_Z(t) = E(t).h, \tag{7}$$

where h is the photostrictive actuator's thickness.

2.2. Constitutive equations

Photostriction is a complex multi-physics problem as a mechanical, electrical, and thermal field are stimulated by the exposure of photostrictive material to light irradiation. Therefore, in the linear theory of photostrictive material, Gibbs free energy density (G) is a function of strain (ε), electric field (E), and temperature (θ). The mathematical expression for electrical Gibbs free energy density can be written as, [37,38].

$$G = \frac{1}{2}Q_{ijkl}\varepsilon_{ij}\varepsilon_{kl} - \frac{1}{2}b_{ij}E_iE_j - \frac{1}{2}\alpha_v\theta^2 - e_{ijk}\varepsilon_{ij}E_k - p_i\theta E_i - \lambda_{ij}\varepsilon_{ij}\theta \tag{8}$$

where Q is the stiffness tensor, e is the piezoelectric stress coefficient tensor, and θ is the temperature rise from ambient temperature (θ_0). The subscript i, j, k, and l take values from 1 to 3. Primary state variables are strain (ε_{ij}), electric field (E_i), and temperature θ, while the associated state variables like stress σ_{ij}, electric displacement (D_i), and entropy density (ϵ) can be obtained as,

$$\sigma_{ij} = \frac{\partial G}{\partial \varepsilon_{ij}}, D_i = -\frac{\partial G}{\partial E_i}, \epsilon = -\frac{\partial G}{\partial \theta}, \text{where} i, j = 1, 2, 3. \tag{9}$$

Therefore, the constitutive equation of the photostrictive actuator

Table 1
Boundary conditions to evaluate effective properties.

	A^-	A^+	B^-	B^+	C^-	C^+	
Eff. Coeff.	$u_i/\varnothing/\theta$	$u_i/\varnothing/\theta$	$u_i/\varnothing/\theta$	$u_i/\varnothing/\theta$	$u_i/\varnothing/\theta$	$u_i/\varnothing/\theta$	Formula
Q_{11}^{eff}	0/-/-	$\widetilde{u}_1$ /-/-	0/-/-	0/-/-	0/0/-	0/0/-	$\overline{\sigma}_{11}/\overline{\varepsilon}_{11}$
Q_{12}^{eff}	0/-/-	$\widetilde{u}_1$/-/-	0/-/-	0/-/-	0/0/-	0/0/-	$\overline{\sigma}_{22}/\overline{\varepsilon}_{11}$
Q_{13}^{eff}	0/-/-	0/-/-	0/-/-	0/-/-	0/0/-	$\widetilde{u}_3$ /0/-	$\overline{\sigma}_{11}/\overline{\varepsilon}_{33}$
Q_{33}^{eff}	0/-/-	0/-/-	0/-/-	0/-/-	0/0/-	$\widetilde{u}_3$ /0/-	$\overline{\sigma}_{33}/\overline{\varepsilon}_{33}$
Q_{44}^{eff}	$\widetilde{u}_3$ /0/-	$\widetilde{u}_3$/0/-	0/-/-	0/-/-	$\widetilde{u}_1$/-/-	$\widetilde{u}_1$ /-/-	$\overline{\sigma}_{13}/\overline{\varepsilon}_{31}$
Q_{66}^{eff}	$\widetilde{u}_2$/-/-	$\widetilde{u}_2$/-/-	$\widetilde{u}_1$/-/-	$\widetilde{u}_1$/-/-	0/0/-	0/0/-	$\overline{\sigma}_{12}/\overline{\varepsilon}_{12}$
e_{13}^{eff}	0/-/-	0/-/-	0/-/-	0/-/-	0/0/-	$0/\widetilde{\phi}$/-	$-\overline{\sigma}_{11}/\overline{E}_1$
e_{33}^{eff}	0/-/-	0/-/-	0/-/-	0/-/-	0/0/-	$0/\widetilde{\phi}$/-	$-\overline{\sigma}_{33}/\overline{E}_1$
e_{15}^{eff}	$\widetilde{u}_3$/0/-	$\widetilde{u}_3$/0/-	0/-/-	0/-/-	$\widetilde{u}_1$/-/-	$\widetilde{u}_1$/-/-	$\overline{D}_1/\overline{\varepsilon}_{31}$
b_{11}^{eff}	0/0/-	$0/\widetilde{\phi}$/-	0/-/-	0/-/-	0/-/-	0/-/-	$\overline{D}_1/\overline{E}_1$
b_{33}^{eff}	0/-/-	0/-/-	0/-/-	0/-/-	0/0/-	$0/\widetilde{\phi}$/-	$\overline{D}_3/\overline{E}_3$
α^{eff}	-/-/$\widetilde{\theta}$	-/-/$\widetilde{\theta}$	-/-/$\widetilde{\theta}$	-/-/$\widetilde{\theta}$	$0/0/\widetilde{\theta}$	-/0/$\widetilde{\theta}$	$\overline{\varepsilon}_{11}$
p^{eff}	-/-/-	-/-/-	-/-/-	-/-/-	-/0/θ^*	-/0/-	$\frac{I}{A.\frac{d\theta}{dt}}$

Where $\widetilde{u}_i$, $\widetilde{\phi}$, and $\widetilde{\theta}$ refers to the nonzero displacement, electric potential, and temperature respectively, - represents the non prescribed values, 0 refers to the zero value of displacement or electric potential, and θ^* refers to the applied sinusoidal variation of temperature on RVE surface.

must incorporate all aforementioned physics and these can be given as,

$$\{\sigma\} = [Q]\{\varepsilon\} - [e]^t\{E\} - [\lambda]\ \{\theta\}, \tag{10}$$

$$\{D\} = [e]\{\varepsilon\} + [b]\{E\} + [p\ ]\{\theta\}, \tag{11}$$

$$\{\in\} = [\lambda]\{\varepsilon\} + [p]\ \{E\} + [\alpha_v]\{\theta\}, \tag{12}$$

where {}, and [] refers to the vector and tensor quantity. $\{\sigma\}$ is stress vector, $[Q]$ is stiffness tensor, $\{\varepsilon\}$ is strain vector, $[e]$ is piezoelectric stress coefficient's tensor, $\{\theta\}$ is a vector containing temperature rise from ambient temperature, $\{D\}$ is the electrical displacement vector, $\{\in\}$ contains entropy density, $\{\lambda\}$ contains thermal stress coefficients, and $[\alpha_v]$ is a material constant $\left(\alpha_v = \rho_m c_m \theta^{-1}\right)$.

2.3. Numerical homogenization

The best way to speed up the process of evaluating overall effective properties is homogenization. This method determines a global homogenized medium that is equivalent to the original composite such that the strain energy stored in both is the same [33]. Firstly, to evaluate the macroscopic effective properties of particle or fiber composites, an RVE is created for both types of composites as shown in Fig. 2. These RVE can capture the geometric and material characteristics of original composites. To generate periodic cubic RVE of spherical particle composite, a random sequential adsorption algorithm (RSA) [33] is used. This algorithm makes sure that there is no overlapping of any two spherical particles. The distance between the center of two particles is $2\times r + s$, where r is the radius of the particle and s is the minimum distance between two particles. An example of particle composite's RVE with 18 % particle's volume fraction is illustrated in Fig. 2a. For the fiber composite two types of arrangements are considered i.e., square, and hexagonal. The RVE of fiber composite, when fibers are arranged in square & hexagonal manner, and their volume fraction is 18 % is shown in Fig. 2b and 2c respectively.

Considering the composites to be transversely isotropic, therefore the constitutive Equations (10–12), can be rewritten in matrix form as mentioned in Equation (13). It can be observed from the matrix Equation (13), that 15 independent effective properties (i.e., 7 elastic, 2 electrical, 3 electromechanical, 2 thermoelastic, and 1 pyroelectric) are needed to be determined to define the overall behavior of the photostrictive composites.

$$\begin{bmatrix} \overline{\sigma}_{11} \\ \overline{\sigma}_{22} \\ \overline{\sigma}_{33} \\ \overline{\sigma}_{23} \\ \overline{\sigma}_{31} \\ \overline{\sigma}_{12} \\ \overline{D}_1 \\ \overline{D}_2 \\ \overline{D}_3 \\ \overline{\in} \end{bmatrix} = \begin{bmatrix} Q_{11}^{eff} & Q_{12}^{eff} & Q_{13}^{eff} & 0 & 0 & 0 & 0 & 0 & -e_{13}^{eff} & \lambda_1^{eff} \\ Q_{12}^{eff} & Q_{11}^{eff} & Q_{13}^{eff} & 0 & 0 & 0 & 0 & 0 & -e_{13}^{eff} & \lambda_1^{eff} \\ Q_{13}^{eff} & Q_{13}^{eff} & Q_{33}^{eff} & 0 & 0 & 0 & 0 & 0 & -e_{33}^{eff} & \lambda_3^{eff} \\ 0 & 0 & 0 & Q_{44}^{eff} & 0 & 0 & 0 & -e_{15}^{eff} & 0 & 0 \\ 0 & 0 & 0 & 0 & Q_{44}^{eff} & 0 & -e_{15}^{eff} & 0 & 0 & 0 \\ 0 & 0 & 0 & 0 & 0 & Q_{66}^{eff} & 0 & 0 & 0 & 0 \\ 0 & 0 & 0 & 0 & e_{15}^{eff} & 0 & b_{11}^{eff} & 0 & 0 & p^{eff} \\ 0 & 0 & 0 & e_{15}^{eff} & 0 & 0 & 0 & b_{11}^{eff} & 0 & p^{eff} \\ e_{13}^{eff} & e_{13}^{eff} & e_{33}^{eff} & 0 & 0 & 0 & 0 & 0 & b_{33}^{eff} & p^{eff} \\ \lambda_1^{eff} & \lambda_1^{eff} & \lambda_3^{eff} & 0 & 0 & 0 & p^{eff} & p^{eff} & p^{eff} & \alpha_v^{eff} \end{bmatrix} \begin{bmatrix} \overline{\varepsilon}_{11} \\ \overline{\varepsilon}_{22} \\ \overline{\varepsilon}_{33} \\ \overline{\varepsilon}_{23} \\ \overline{\varepsilon}_{31} \\ \overline{\varepsilon}_{12} \\ \overline{E}_1 \\ \overline{E}_2 \\ \overline{E}_3 \\ \overline{\theta} \end{bmatrix}, \tag{13}$$

where $\overline{A}$ is the mean value of property A. Composites can be obtained by periodic placement of RVEs in three dimensions. Therefore, to ensure that each RVE has the same mode of deformation and there is no overlapping or separation between neighboring RVEs, RVE must be subjected to periodic boundary conditions.

Periodic boundary conditions on the surface of the RVE in cartesian coordinates were put forward by Suquet [39]. The displacement at each node on the opposite surfaces of the RVE can be given as,

$$u_i^{K^+} = \overline{\varepsilon}_{ij} x_j^{K^+} + v_i^{K^+}, \tag{14}$$

$$u_i^{K^-} = \overline{\varepsilon}_{ij} x_j^{K^-} + v_i^{K^-}, \tag{15}$$

where u_i is the displacement in direction i (i.e., $i = 1$, 2, and 3), v_i is the local fluctuation of the displacement on the RVE surface that depends on the global load applied, and K^+/K^- refers to the pair of opposite surfaces of the RVE in x_j direction. K^+/K^- is equal to A^+/A^-, B^+/B^-, and C^+/C^- when $j = 1$, 2, and 3 respectively, as shown in Fig. 2. As the local fluctuation is equal on the two opposite surfaces, therefore subtracting Equations (14) and (15) will give conditions for applied macroscopic strain.

$$u_i^{K^+} - u_i^{K^-} = \overline{\varepsilon}_{ij}\left(x_i^{K^+} - x_i^{K^-}\right). \tag{16}$$

Similarly, boundary conditions to apply macroscopic electric field can be given as,

$$\varnothing^{K^+} - \varnothing^{K^-} = \overline{E}_i\left(x_i^{K^+} - x_i^{K^-}\right). \tag{17}$$

Moreover, the mean value of any property $(\overline{A})$ can be calculated by taking the volume average of property A at every node in the RVE,

$$\overline{A} = \frac{1}{V}\int_V A dV, \tag{18}$$

where V refers to volume of the RVE. Considering Equations (16) and (17) periodic boundary conditions are applied to the RVE. Evaluation of all effective properties is conducted by applying the boundary conditions [28,29,40] specified in Table 1.

3. Finite element formulation

Oftentimes finite element method has been employed to investigate static and dynamic response of the laminated composite structures [41,42]. This section presents the finite element formulation for the static and dynamic response of laminated structures while considering that the photostrictive actuators are perfectly bonded to the host structure. The effect of bonding material is neglected. First-order shear

deformation theory (FSDT) is used with a four-noded degenerated shell element to model the laminated structure. Every node has six mechanical, one electrical, and one thermal degree of freedom.

3.1. Geometry and displacement field

The coordinate of any arbitrary point in k^{th} layer of degenerated shell element can be written with the help of the shape function N_i and thickness,

$$\begin{Bmatrix} x \\ y \\ z \end{Bmatrix} = \sum_{i=1}^{4} N_i \begin{Bmatrix} x_i \\ y_i \\ z_i \end{Bmatrix} + \sum_{i=1}^{4} N_i H_i \begin{Bmatrix} l_{3i} \\ m_{3i} \\ n_{3i} \end{Bmatrix}, \tag{19}$$

where x_i, y_i, and z_i are global coordinates of mid-surface in the 1, 2, and 3 direction at any node *i*. l_{3i}, m_{3i}, and n_{3i} are the direction cosines of the normal vector V_{3i} at any node *i*. H_i is given in Annexure A, as Equation (A.1). Therefore, displacement at any point in the k[th] layer of degenerated shell element can be given using the three mid-surface displacements (u_{oi}, v_{oi}, and w_{oi}) and two rotations (α_i and β_i) as

$$\begin{Bmatrix} u \\ v \\ w \end{Bmatrix} = \sum_{i=1}^{4} N_i \begin{Bmatrix} u_{oi} \\ v_{oi} \\ w_{oi} \end{Bmatrix} + \sum_{i=1}^{4} N_i H \begin{bmatrix} l_{1i} & -l_{2i} \\ m_{1i} & -m_{2i} \\ n_{1i} & -n_{2i} \end{bmatrix} \begin{Bmatrix} \alpha_i \\ \beta_i \end{Bmatrix}, \tag{20}$$

where l_{1i}, m_{1i}, and n_{1i} are the direction cosines of the tangential vector V_{1i} at node *i*. l_{2i}, m_{2i}, and n_{2i} are the direction cosines of the tangential vector V_{2i} at node *i*. α_i and β_i are rotation about V_{1i} and V_{2i} respectively.

3.2. Strain displacement relationship

The strain vector $\{\varepsilon\}$ can be obtained by taking the partial derivative of a displacement vector $\{u \quad v \quad w\}^t$, which can be written as,

$$\{\varepsilon\}_e = \begin{Bmatrix} \varepsilon_x \\ \varepsilon_y \\ \varepsilon_z \\ \gamma_{xy} \\ \gamma_{yz} \\ \gamma_{zx} \end{Bmatrix}_e = \begin{Bmatrix} \frac{\partial u}{\partial x} \\ \frac{\partial v}{\partial y} \\ \frac{\partial w}{\partial z} \\ \frac{\partial u}{\partial y} + \frac{\partial v}{\partial x} \\ \frac{\partial v}{\partial z} + \frac{\partial w}{\partial y} \\ \frac{\partial w}{\partial x} + \frac{\partial u}{\partial z} \end{Bmatrix}_e = [B]_e \{q\}_e, \tag{21}$$

where elemental strain displacement matrix $[B]_e$ is given in Annexure A, as Equation (A.2). $\{q\}_e$ is the elemental displacement vector. Under the plane stress consideration, stress–strain relationship can be given as,

$$\{\sigma\}_e = [Q^{'}]_e \{\varepsilon\}_e, \tag{22}$$

where $[Q^{'}]_e$ is the elemental reduced material matrix, which is given in Annexure A, as Equation (A.4).

3.3. Electric field

The current study considers that the electric field functions in the thickness direction of a photostrictive actuator and the electric effect is constant in a layer of the element. Therefore, the electric field inside the k^{th} layer within an element can be written as.

$$\{E\}_k = -\{B_\phi\}_e \phi_{pk}, \tag{23}$$

where ϕ_{pk} is the electric potential of the k[th] photostrictive layer and $\{B_\phi\}_e$ is given in Annexure A, as Equation (A.6).

3.4. Thermal field

It is assumed that the temperature is constant in an element, which leads to only one thermal degree of freedom per element. It is also considered that the temperature gradient *G* exist only in the thickness direction. Mathematically temperature gradient can be given as.

$$\{G\}_k = -\{B_\theta\}_e \theta_{P_k}, \tag{24}$$

where θ_{P_k} is the temperature of k^{th} photostrictive layer and $\{B_\theta\}_e$ is given in Annexure A, as Equation (A.7). Transforming the constitutive Equations (10)-(12) from material principle direction to the global coordinate system, then the equation can be given as,

$$\{D\}_k = [\overline{e}]_k \{\varepsilon\}_k + [\overline{b}]_k \{E\}_k + \{\overline{p}\}_k \{\theta\}_k, \tag{25}$$

$$\{\sigma\}_k = [\overline{Q}]_k \{\varepsilon\}_k - [\overline{e}]_k^T \{E\}_k - \{\overline{\lambda}\}_k \{\theta\}_k, \tag{26}$$

$$\{\epsilon\} = \{\overline{\lambda}\}_k^T \{\varepsilon\}_k + \{\overline{p}\}_k^T \{E\}_k + \alpha_v \{\theta\}_k, \tag{27}$$

where, $[\overline{e}]_k$, $[\overline{b}]_k$, $\{\overline{p}\}_k$, $[\overline{Q}]_k$, and $\{\overline{\lambda}\}_k$ are given in Annexure A in Equations (A.8) and (A.9).

3.5. Strain energy

Due to elastic deformation, the strain energy *V* will get stored in the structure and it can be mathematically expressed as,

$$V^e = \frac{1}{2} \sum_{k=1}^{npl} \int_V \{\varepsilon\}_e^T \{\sigma\}_{p_k} dV, \tag{28}$$

On substituting for stress and strain from the above formulation, Strain energy can be rewritten as,

$$V^e = \frac{1}{2} \left(\{q\}_e^T [K_{uu}]_e \{q\}_e + \{q\}_e^T [K_{u\phi}]_e \{\phi\}_e - \{q\}_e^T [K_{u\theta}]_e \{\theta\}_e \right), \tag{29}$$

where $[K_{uu}]_e$ is the elemental mechanical stiffness matrix, $[K_{u\phi}]_e$ is the elemental mechanical electrical coupling stiffness matrix, and $[K_{u\theta}]_e$ is the elemental mechanical thermal coupling stiffness matrix. $[K_{uu}]_e$, $[K_{u\phi}]_e$, and $[K_{u\theta}]_e$ are mentioned in Annexure A in Equations (A.13), A.14, and A.15.

3.6. Electrical energy

On subjecting a photostrictive layer to light, electrical energy is produced. Accumulated electrical energy in the photostrictive layer makes it act as a capacitor. Therefore, the electrical energy in an element can be calculated by summing electrical energy in the photostrictive layers, which can be written as,

$$W^e = \frac{1}{2} \sum_{k=1}^{npl} \int_V \{E\}_e^T \{D\}_{p_k} dV. \tag{30}$$

On substituting the equation for electrical field and electric displacement from the above formulation, elemental electrical energy can be written as,

$$W^e = -\frac{1}{2} \{\phi\}_e^T [K_{\phi u}]_e \{q\}_e + \frac{1}{2} \{\phi\}_e^T [K_{\phi\phi}]_e \{\phi\}_e - \frac{1}{2} \{\phi\}_e^T [K_{\phi\theta}]_e \{\theta\}_e, \tag{31}$$

where *npl* represents the total number of photostrictive layers and $[K_{\phi u}]_e$, $[K_{\phi\phi}]_e$, and $[K_{\phi\theta}]_e$ are given in Annexure A in Equations (A.16) – (A.18).

3.7. Thermal energy

Owing to the entropy and temperature rise thermal energy will get stored in the photostrictive layer. The elemental thermal energy can be

determined by adding thermal energy of all the photostrictive layers in an element, which can be mathematically expressed as.

$$V^{\theta} = \frac{1}{2}\sum_{k=1}^{npl}\int_{V} \epsilon^{T}\{\theta\}_{e} dV. \tag{32}$$

Substituting for entropy from the constitutive equation, the elemental thermal energy will become,

$$V^{\theta} = \frac{1}{2}\{q\}_{e}^{T}[K_{u\theta}]_{e}\{\theta\}_{e} - \frac{1}{2}\{\phi\}_{e}^{T}[K_{\phi\theta}]_{e}\{\theta\}_{e} + \frac{1}{2}\{\theta\}_{e}^{T}[H_{\theta\theta}]_{e}\{\theta\}_{e}, \tag{33}$$

where $[K_{u\theta}]_e$, $[K_{\phi\theta}]_e$, and $[H_{\theta\theta}]_e$ is given in Annexure A in Equations (A.15), A.18, and A.19.

3.8. Kinetic energy

Elemental kinetic energy can be expressed as,

$$T^{e} = \frac{1}{2}\sum_{k=1}^{nl}\int_{V} \rho_k\{\dot{\bar{u}}\}^{t}\{\dot{\bar{u}}\} dV \tag{34}$$

where ρ_k represents the density of k^{th} layer. The elemental kinetic energy can be rewritten as,

$$T^{e} = \frac{1}{2}\{\dot{q}\}_{e}^{t}[m_{uu}]_{e}\{\dot{q}\}_{e} \tag{35}$$

where the elemental mass matrix $[m_{uu}]_e$ is given in Annexure A in Equation (A.20).

3.9. Work done by the external forces, electrical charges, and heat flux

Deformation caused by the external forces leads to the mechanical work done, while in the presence of irradiated light and electric field, the electrical charges will do work in the photostrictive layers. Moreover, the incoming and leaving heat flux will also do work in the photostrictive layers. All these works done can be mathematically expressed as,

$$\begin{aligned} W^{s} = &\sum_{k=1}^{nl}\int_{s_1}\{\bar{u}\}_{e}^{T}\{f_s\}_{e} dS + \sum_{k=1}^{nl}\{\bar{u}\}_{e}^{T}\{f_p\} + \sum_{k=1}^{nl}\int_{V}\{\bar{u}\}_{e}^{T}\{f_b\} dV + \sum_{k=1}^{npl} \\ &\times \int_{s_2}\{E\}_{e}^{T}\{f_q\}_{e} dS - \frac{1}{2}\sum_{k=1}^{npl}\int_{V}\{\theta\}_{e}^{T}[B_{\theta}]^{T}[k][B_{\theta}]\{\theta\}_{e} dV + \sum_{k=1}^{npl} \\ &\times \int_{s_3} q_s\{\theta\}_{e}^{T} dS - \sum_{k=1}^{npl}\frac{1}{2}\int_{s_4} h_v\left(\{\theta\}^{2} - 2\{\theta\}\theta_{\infty} + \theta_{\infty}^{2}\right) dS, \end{aligned} \tag{36}$$

where external forces, electrical charges, incoming heat flux, and outgoing heat flux acts on s_1, s_2, s_3 and s_4 respectively. $\{f_s\}_e$ refers to surface traction, $\{f_p\}$ represents point load, $\{f_b\}$ is the body load and $\{f_q\}_e$ is the surface electrical charge density.

3.10. Coupled equations of motion

The global finite element equations for an element are derived by employing Hamilton's principle.

$$\int_{t_1}^{t_2}\left(\delta T^{e} - \delta V^{e} + \delta W^{e} + \delta V^{\theta} + \delta W^{s}\right) dt = 0, \tag{37}$$

where δ is the variational operator. Upon substituting for the kinetic energy T^e, potential energy V^e, electrical energy W^e, thermal energy V^θ and external work done W^s in Equation (37), elemental finite element equations are derived. Assembling all the elemental finite element equations will give global finite element equations, which can be expressed as

$$[M_{uu}]\{\ddot{q}\} + [C_{uu}]\{\dot{q}\} + [K_{uu}]\{q\} + [K_{u\phi}]\{\phi\} - [K_{u\theta}]\{\theta\} = v \tag{38}$$

$$[K_{\phi u}]\{q\} - [K_{\phi\phi}]\{\phi\} + [K_{\phi\theta}]\{\theta\} = \{F_q\}, \tag{39}$$

$$-[K_{\theta u}]\{q\} + [K_{\theta\phi}]\{\phi\} + [K_{\theta\theta}]\{\theta\} - [H_{\theta\theta}]\{\theta\} = \{F_{\theta}\}, \tag{40}$$

where $[M_{uu}]$ is the global mass matrix, $[C_{uu}]$ is the global damping matrix, $[K_{uu}]$ is global elastic stiffness matrix, $[K_{u\phi}]$ is global elastic electric stiffness matrix, $[K_{u\theta}]$ is elastic thermal stiffness matrix, $[K_{\phi\phi}]$ is global electric stiffness matrix, $[K_{\phi\theta}]$ is global electric thermal stiffness matrix, and $[K_{\theta\theta}] - [H_{\theta\theta}]$ is the global thermal stiffness matrix. Whereas $\{F_m\}$, and $\{F_q\}$, $\{F_\theta\}$ are applied mechanical force, electrical charges, and thermal excitation respectively. $\{q\}$, $\{\phi\}$, and $\{\theta\}$ are global displacement, voltage, and temperature vector respectively. The expression to calculate $[C_{uu}]$ is given in Annexure A in Equation A(21).

The current study considers the smart structure with a top and bottom photostrictive layer on the host structure, which acts as an actuator. But only one actuator is active at any instant. Therefore, the Equations (38) – (40) will change to.

$$\begin{aligned} &[M_{uu}]\{\ddot{q}\} + [C_{uu}]\{\dot{q}\} + [K_{uu}]\{q\} + [K_{u\phi}]\{\phi\} \\ &\quad = \{F_m\} + [K_{u\theta}]\{\theta\} - [K_{u\phi_a}]\{\phi_a\}, \end{aligned} \tag{41}$$

$$[K_{\phi_a u}]\{q\} - [K_{\phi_a\phi}]\{\phi_a\} + [K_{\phi_a\theta}]\{\theta\} = \{F_{q_a}\}, \tag{42}$$

$$-[K_{\theta u}]\{q\} + [K_{\theta\phi}]\{\phi_a\} + [K_{\theta\theta}]\{\theta\} - [H_{\theta\theta}]\{\theta\} = \{F_{\theta_a}\}. \tag{43}$$

Displacement and velocity of the host structure at a reference point will be captured by a vibrometer, which will act as input to the controllers. The controller will command the light source to irradiate light over the photostrictive actuator, then electric field and electric potential ϕ_a will be induced, which can be calculated using Equations (2) and (6) respectively. Controlled response $\{q\}$ of the smart structure can be obtained by solving Equation (41). It is a second-order time-dependent equation, which can be solved with the Newmark algorithm. The parameters $\alpha = 1/2$, and $\beta = 1/4$ are considered for an unconditionally stable Newmark scheme.

4. Controller design

A controller is designed to attain the structural vibration to the desired limit employing the actuators within the least time possible. The current study deploys two kinds of controllers i.e., velocity feedback control and fuzzy logic control. The displacement and its change rate (i.e., velocity) of the host structure are considered as inputs to the controllers, whereas the light intensity is the control output.

4.1. Velocity feedback control

This is a simple control strategy where the changing rate of displacement (i.e., velocity) is amplified by multiplying it with some gain to obtain the light intensity I, such as.

$$I = G_v\{\dot{q}_s\}, \tag{44}$$

where G_v is the gain and $\dot{q}_s$ is the changing rate sensed by a laser vibrometer. As, the light intensity cannot be negative therefore the location of light irradiation (i.e., upon top or bottom photostrictive actuator) will be decided by the direction of the displacement sensed by the vibrometer.

4.2. Fuzzy logic control

A fuzzy logic controller can be used to control complex systems as it mimics the human mind and it does not require any complex mathe-

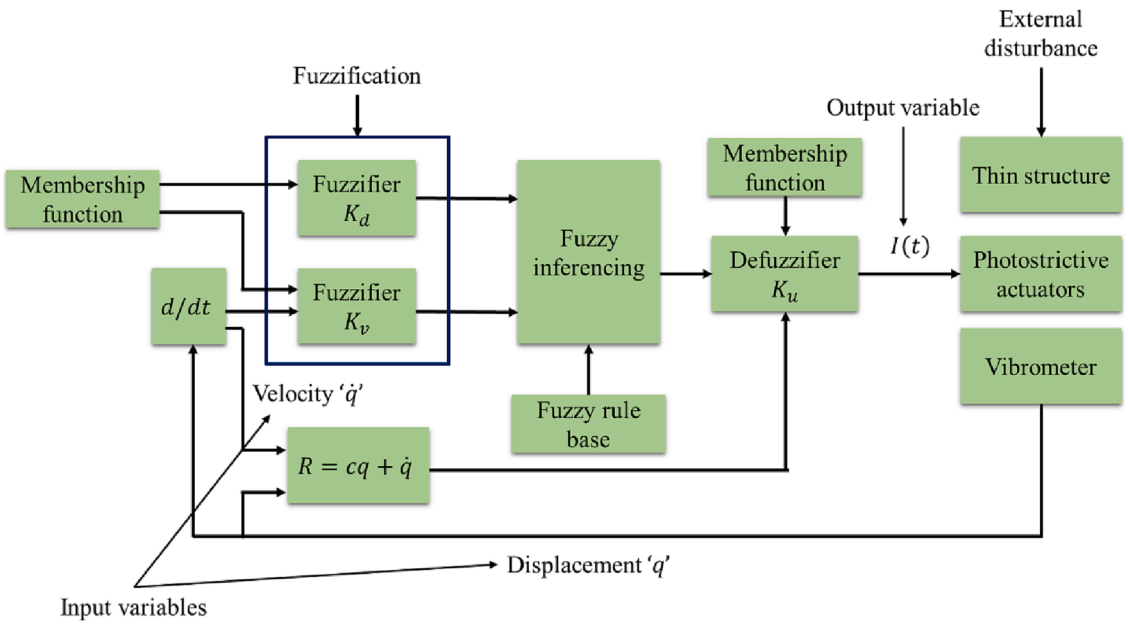

Fig. 3. Schematic of fuzzy logic controller.

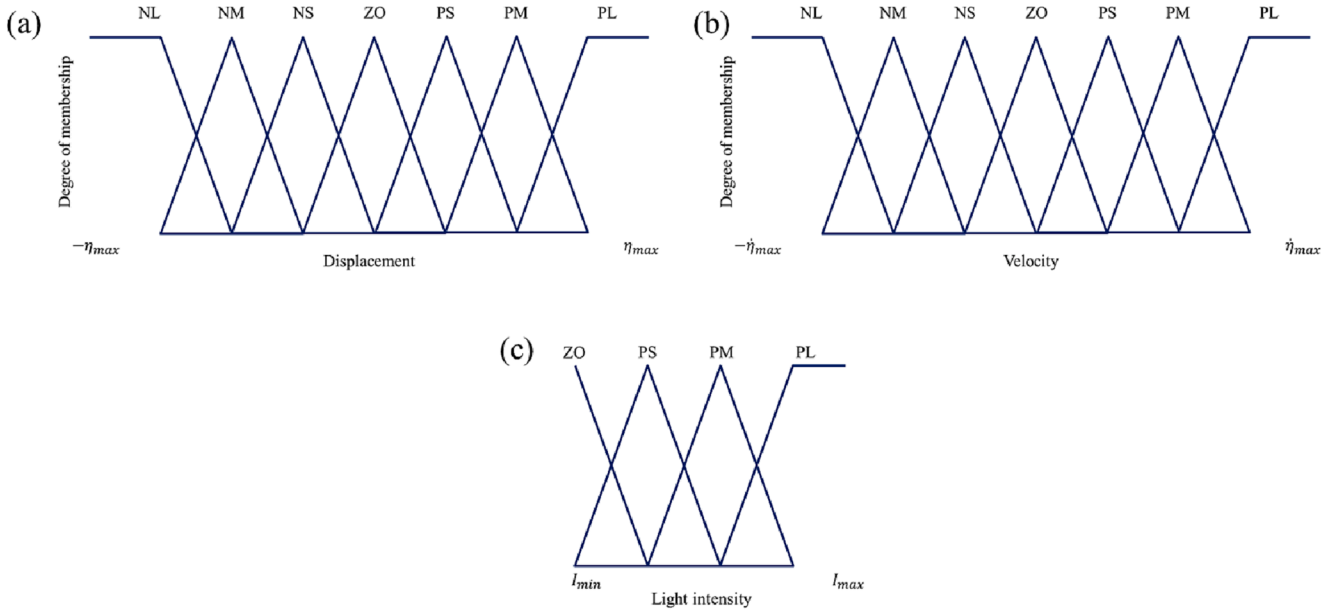

Fig. 4. Membership function for input variables (a) displacement, (b) velocity and for output variable (c) light intensity.

Table 2
Fuzzy control rules.

q	$\dot{q}$						
	NL	NM	NS	ZO	PS	PM	PL
NL	PL	PL	PL	PM	ZO	ZO	ZO
NM	PL	PL	PL	PS	ZO	ZO	PS
NS	PL	PL	PL	ZO	ZO	PS	PM
ZO	PL	PM	PS	ZO	PS	PM	PL
PS	PM	PS	ZO	ZO	PL	PL	PL
PM	PS	ZO	ZO	PS	PL	PL	PL
PL	ZO	ZO	ZO	PM	PL	PL	PL

Table 3
Material properties of PLZT photostrictive actuator.

Property	Symbol	Value
Voltage leakage constant	β	0.01 V/s
Heat capacity	H	16 W/°C
Saturated electric field	E_s	7.29×10^5 V/m
Pyroelectric constant	p	0.23×10^3 C/m^2 °C
Optical actuator constant	$\alpha^{'}$	0.02772 cm^2/(Ws)
Electric permittivity	ε	1.65×10^{-8} F/m
Power of absorbed Heat	P^{*}	0.23×10^3 cm^2/s
Heat transfer rate	γ	0.915 W/°C s
Piezoelectric strain constant	d_{33}	1.79×10^{-10} m/V

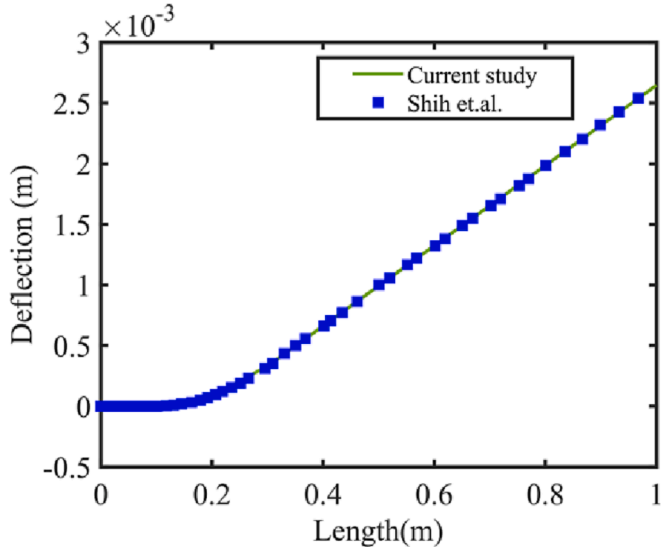

Fig. 5. Static validation of deflection response of a cantilever beam bonded with PLZT photostrictive material.

matical model to take a decision [43]. A fuzzy logic controller converts the input into vague terms and then implements an expert's knowledge base to decide the control signal. This control signal is again converted into a crisp output value. This section designs the fuzzy logic controller to control the flexible structure with bonded top and bottom photostrictive actuator. A fuzzy logic control system is a close loop controller as shown in Fig. 3. A fuzzy logic control unit consists of a fuzzifier, fuzzy rule base, fuzzy inferencing, and at last defuzzification, as shown in Fig. 3. The current study considers the displacement q and changing rate of displacement $\dot{q}$ (i.e., velocity) of the reference point measured by the remote laser vibrometer as fuzzy inputs. These designated inputs are then multiplied by the quantization factors K_d and K_v to transform them into their respective domain, as shown in Fig. 3. These input values are then converted into fuzzy values via fuzzification as shown in Fig. 3. Then using a rule base table corresponding to the fuzzy values of input a control signal will be selected, this process is known as fuzzy inferencing, as shown in Fig. 3. This control signal will be converted into a crisp value using membership functions also known as defuzzification. The control crisp value is multiplied by K_u to obtain the desired light intensity output $I(t)$. As the vibration displacement decreases very near to zero, the fuzzy logic controller should be able to analyze the small displacement changes. Therefore, to improve the real-time self-tuning of the controller the quantization factors K_d and K_v can be expressed as,

$$K_d = \frac{3}{q}, \text{and} K_v = \frac{1}{q\omega}, \tag{45}$$

where ω is the natural frequency. In the later stage, when the vibration has already been attenuated enough, then there is no need to apply control force. Therefore, Light intensity should approach zero, hence the fuzzified tuning factor K_u can be evaluated as

$$K_u = \frac{|R|}{|R| + \delta} \cdot \frac{I_{max}}{3}, \tag{46}$$

where $|R|$ refers to the absolute value of the light switching function $R = cq + \dot{q}, c = \zeta\omega, \zeta$ is the host structure damping ratio, δ is a small positive constant and I_{max} is the maximum irradiated light intensity. A fuzzy controller can be designed as,

(1) Defining linguistic variables and membership functions.

The inputs selected for this control system are the displacement and velocity of the reference point, which are defined in the universe of

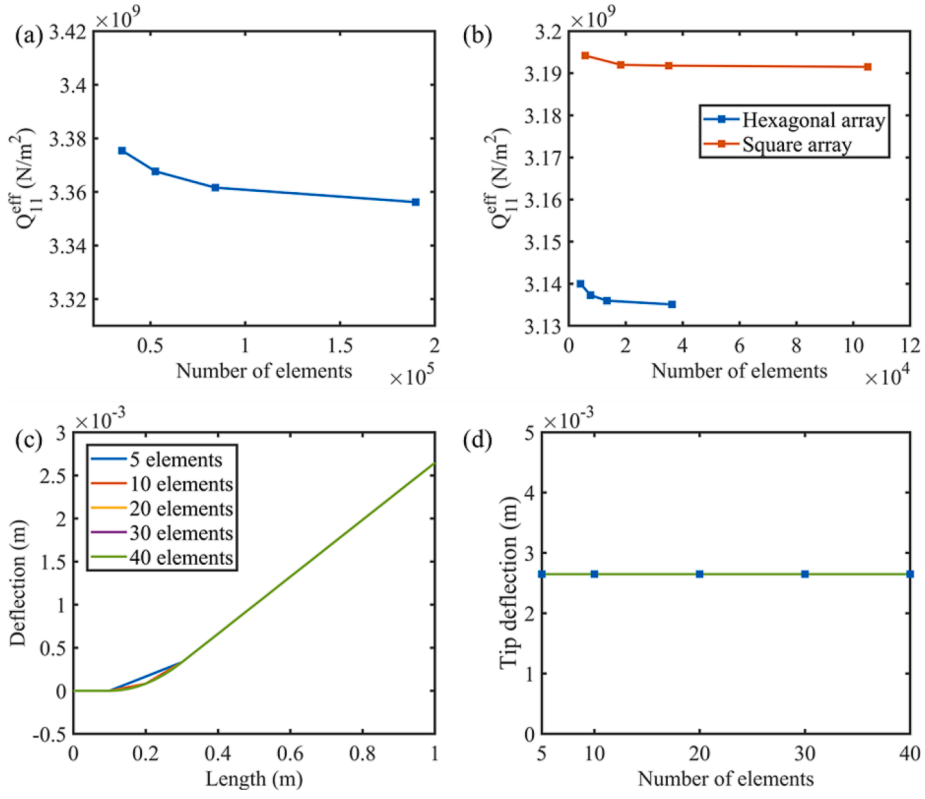

Fig. 6. Convergence analysis of Q_{11}^{eff} (a) particulate composite, (b) fiber composite with 24 % inclusion volume fraction, (c) Deflection response, and (d) tip deflection of cantilever attached to PLZT while performing the mesh refinement.

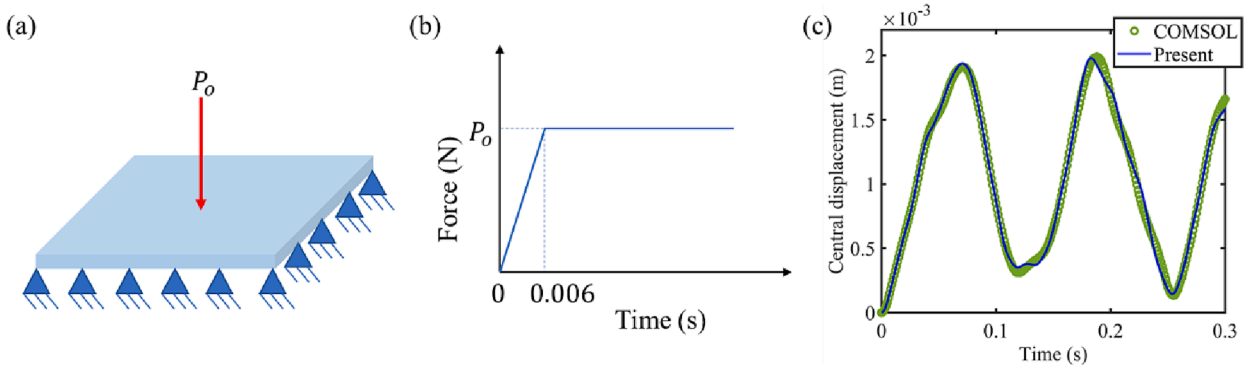

Fig. 7. (a) square plate subjected to Clamped boundary condition on all sides and (b) step force at the center and (c) its dynamic transverse center deflection.

Table 4
Comparison of natural frequency.

h/a	Boundary conditions		No. of element	$\bar{\omega}$
0.01	CCCC	Ferreira [44]	25 × 25	0.1761
		Present FEM	9 × 9	0.1751
		Analytical [44]		0.1754
0.1	CCCC	Ferreira [44]	20 × 20	1.5996
		Present FEM	10 × 10	1.5995
		Analytical [44]		1.594
0.01	SSSS	Ferreira [44]	25 × 25	0.0965
		Present FEM	6 × 6	0.09594
		Analytical [44]		0.0.0963
0.1	SSSS	Ferreira [44]	20 × 20	0.9327
		Present FEM	6 × 6	0.93127
		Analytical [44]		0.93

Table 5
Properties of constituting materials of photostrictive composite.

Property	Materials	
	PTB7-Th	PMN-35PT [45]
E_1 (Pa)	0.8×10^9 [46]	7.58×10^{10}
E_3 (Pa)	0.8×10^9 [46]	6.81×10^{10}
υ_{12}	0.43 [46]	0.300136
υ_{13}	0.43 [46]	0.458368
d_{31} (m/V)	–	-2.15×10^{-10}
$\varepsilon_{11}^s/\varepsilon_0$	3.4 [47]	1650
$\varepsilon_{33}^s/\varepsilon_0$	3.4 [47]	2649.762
$\alpha(C^{-1})$	6.5×10^{-4} [48]	3.2×10^{-6} [49]
p (C/m^2K)	–	3×10^{-4} [50]
$\rho(Kg/m^3)$	1.33×10^3 [51]	8.06×10^3
c_p (J/Kg.K)	1.2917×10^3 [52]	3.2×10^2 [53]
k (W/m.K)	0.2 [48]	1.43 [53]

discourse [−3 3], and [-13 13] respectively. The selected output is the light intensity and its universe of discourse is [0 3] because the light intensity can not be negative. The inputs can be classified using a set of linguistic values i.e., {NL, NM, NS, ZO, PS, PM, PL}, and the set of linguistic values for output is {ZO, PS, PM, PL}. Moreover, NL, NM, NS, ZO, PS, PM, and PL represents negative large, negative medium, negative small, zero, positive small, positive medium, and positive large respectively. Both triangular and trapezoidal membership functions (as shown in Fig. 4) are used to fuzzify the input and output values on the set universe of discourse.

(2) Defining fuzzy control rules.

Fuzzy control rules are used to select the control signal based on set rules. These rules are generally based on expert control experiences. Relying on the past vibration control problem experience, it has been found that when $q < 0$ and $\dot{q} < 0$, control force should be more. A photostrictive actuator can produce a large control force when irradiated with high light intensity, therefore the corresponding linguistic term for output variable is PL. Similarly, when $q > 0$ and $\dot{q} > 0$, selected linguistic term for output variable should be PL. However, when $q < 0$ and $\dot{q} > 0$ or $q > 0$ and $\dot{q} < 0$, therefore small or very small control force is required and the corresponding output linguistic variables should be ZO, PS, or PM. As per the aforementioned experience, the fuzzy control rules are designed and mentioned in Table 2.

(3) Defuzzification.

After fuzzy inferencing the output variable is in fuzzy linguistic form, therefore to obtain a crisp output value, the defuzzification of linguistic terms should be carried out using the aggregation method. The present formulation utilizes the centroid method to defuzzify the linguistic term into a crisp output value. Expression for output evaluated using centroid method is.

$$I^{'}(t) = \sum_{i=1}^{m} \frac{w^i y^i}{w^i}, \tag{47}$$

$$I(t) = K_u I'(t) \tag{48}$$

where m is the number of rules for every inference. $y^i \in R$ refers to a point where $\mu\left(I^{'}(t)^i\right)$ achieves its maximum value, $w^i = min(\mu(q), \mu(\dot{q}))$, and μ is the membership value [43].

The current study uses the 47 linguistic fuzzy variables for both displacement and velocity, to improve the control effect. Therefore, the fuzzy control table used in control operation has 47^2 rules. For the displacement's universe of discourse, 10 points are selected between [−3, −1] and [1,3] with a step of 0.5, 18 points are selected between [−0.9, −0.1] and [0.1, 0.9] with a step of 0.1, and 19 points are selected between [−0.09, 0.09] with a step size of 0.01. In the velocity's universe of discourse, 10 points are selected between [−13, −1] and [1,13] with a step of 0.5, 18 points are selected between [−0.9, −0.1] and [0.1, 0.9] with a step of 0.1, and 19 points are selected between [−0.09, 0.09] with a step size of 0.01. This helps to enhance the control effect.

5. Numerical simulation results and discussion

The mathematical formulation mentioned in Section 3 is implemented into computer code using the MATLAB platform. The formulation presented in the current work is validated for the static and dynamic responses before carrying out the desired investigations.

5.1. Static validation

For static validation, the deflection response of a cantilever beam bonded with a photostrictive actuator is compared to the literature [35].

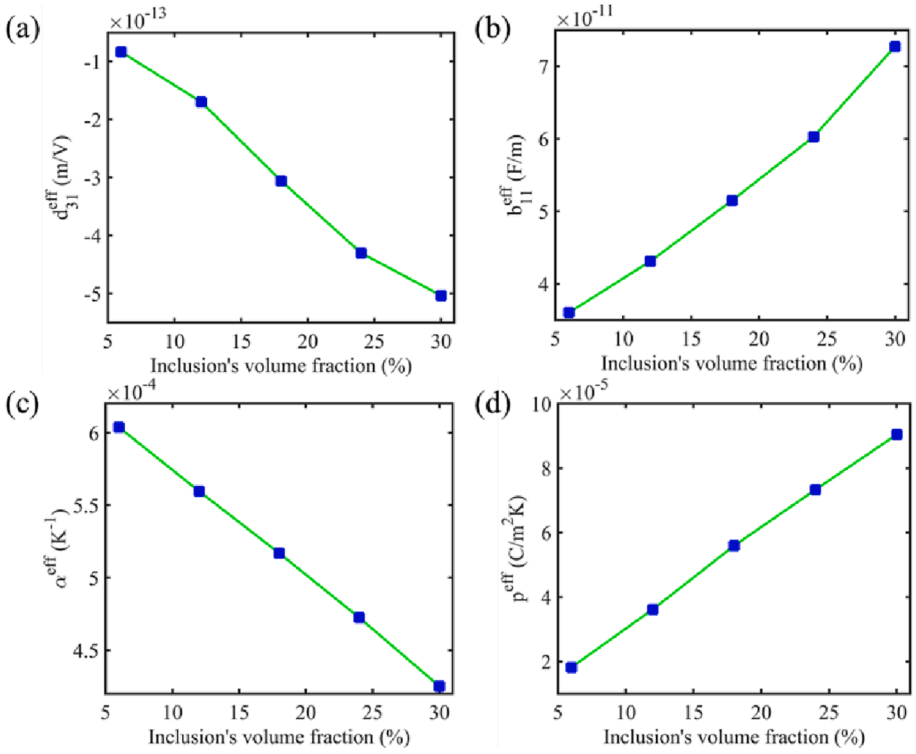

Fig. 8. Variation of effective (a) piezoelectric coupling coefficient, (b) dielectric constant, (c) thermal expansion coefficient, and (d) pyroelectric coefficient properties of the particulate composite when the volume fraction of inclusion varies from 6 % to 30 %.

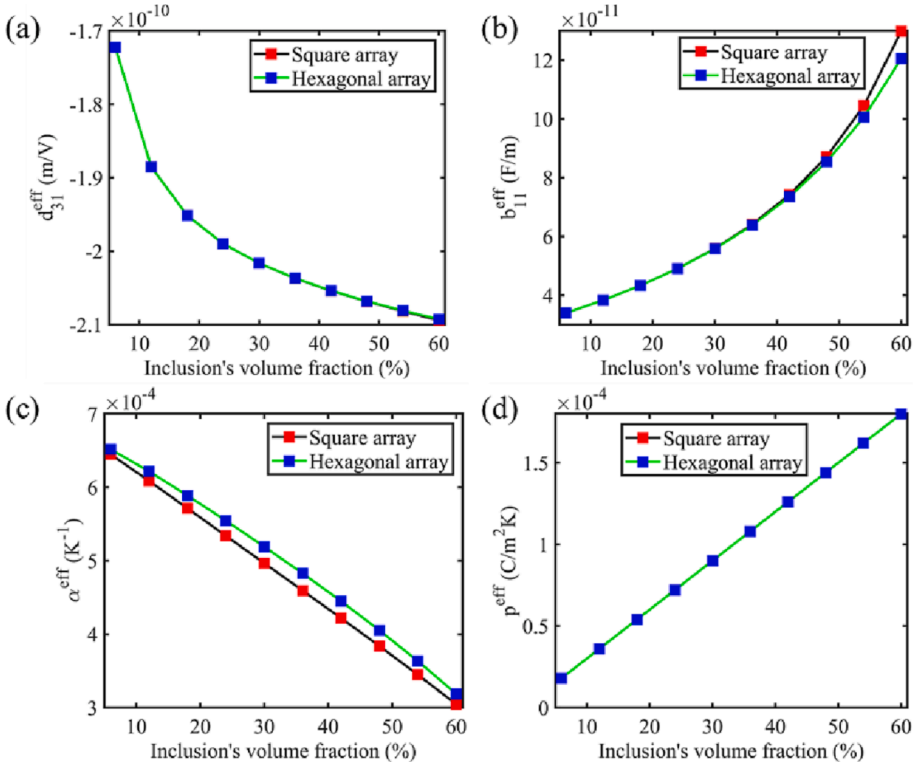

Fig. 9. Variation of effective (a) piezoelectric coupling coefficient, (b) dielectric constant, (c) thermal expansion coefficient, and (d) pyroelectric coefficient properties of fiber composite when the volume fraction of inclusion varies from 6 % to 60 %.

A cantilever beam of dimension $1 \times 0.03 \times 0.002$ m is discretized with 10×1 elements, on this cantilever beam a patch of photostrictive material is attached at a distance of 0.2 m from its center to the fixed end. The dimensions of the photostrictive patch are $0.2 \times 0.03 \times 0.0003$ m. This photostrictive actuator is subjected to 60 mW/cm^2 light irradiation. The host structure is made up of mild steel, which has Young's Modulus

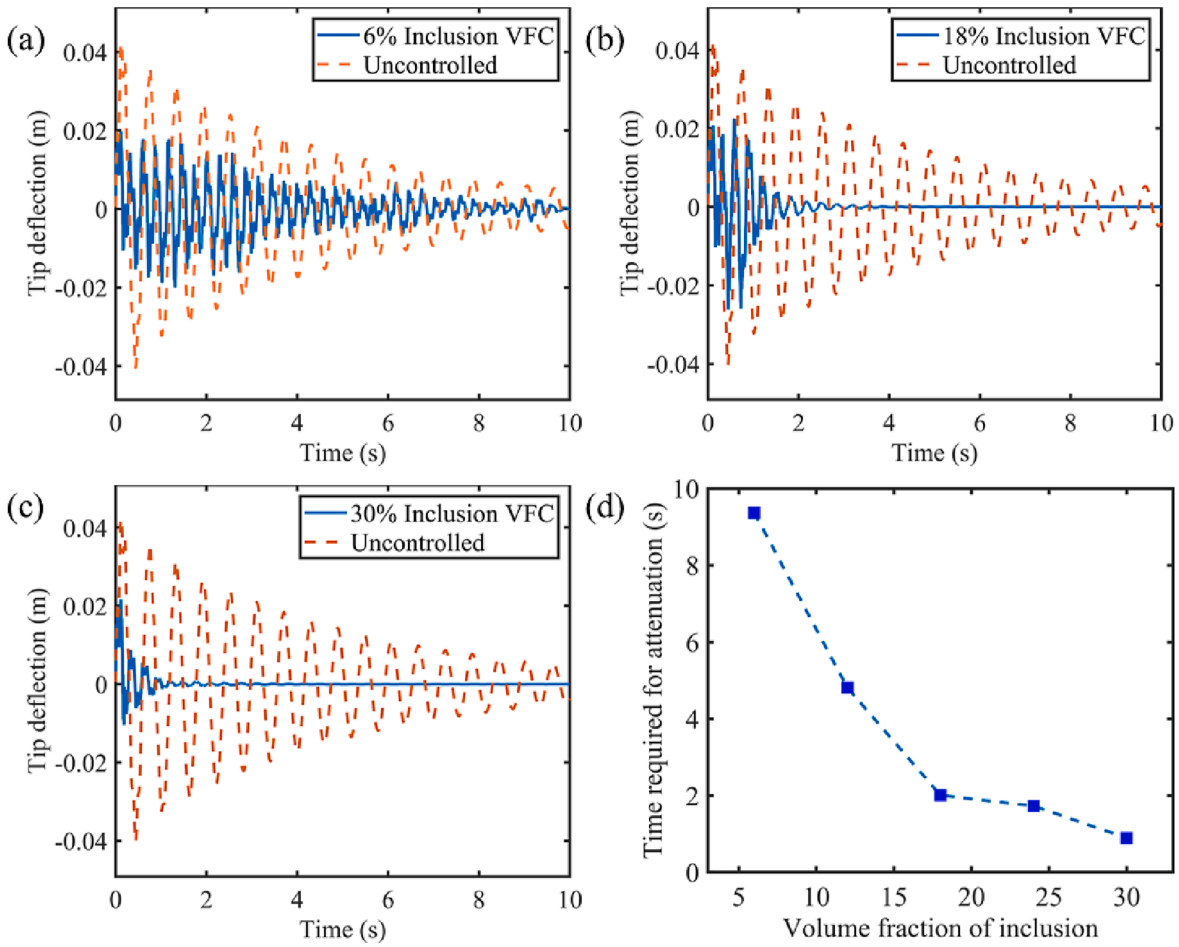

Fig. 10. Vibration response of velocity feedback-controlled cantilever structure when bonded with photostrictive particulate composite of inclusion's volume fraction (a) 6 %, (b) 18 %, (c) 30 %, and (d) time required to achieve approximately 95 % vibration attenuation.

$E = 2.1 \times 10^{11}$ N/m^2 and density $\rho = 7.8 \times 10^3$ kg/m^3. The photostrictive actuator's material is PLZT and its material properties are enlisted in Table 3.

By observing Fig. 5, it can be stated that the deflection response determined utilizing the current formulation is in concurrence with the literature [35].

5.2 Convergence study

Two convergence studies have been conducted first to ensure there is no effect of refined mesh on effective properties and secondly employing the current finite element formulation to the cantilever beam attached to PLZT photostrictive actuator. Fig. 6a and 6b represent an example of the convergence of effective stiffness property Q_{11}^{eff} for particulate composite and fiber composite, when the inclusion volume fraction is 24 %. The number of elements at which convergence is achieved is used in the subsequent simulations respectively. For the convergence study of the current cantilever beam with a photostrictive patch, the element in Y direction is unity, whereas the number of elements in the X direction is varied from 5 to 40, to investigate its effect on cantilever beam's deflection. All the material properties, boundary conditions, and light irradiation are the same as mentioned in Section 5.1. It can be observed from Fig. 6c that refining the mess has an effect only on deflection under the actuator's position, while the tip deflection remains constant (see Fig. 6d). Therefore it is prudent to say that the current formulation provides appropriate convergence.

5.3. Dynamic validation

The dynamic behavior of a plate under center impact load is studied with the current formulation mentioned in Section 2 and the obtained dynamic response is compared with COMSOL. The schematic geometry of the plate under study is shown in Fig. 7a, and of impact load in Fig. 7b. The plate is clamped on all sides and the dimensions of the plate are $1.016 \times 1.524 \times 0.0254$ m. A finite element mesh of 32×32 is considered to discretize the plate. The material properties of the plate are Young's modulus $E = 2.0955 \times 10^8$ N/m^2, Poisson's ratio $\upsilon = 0.25$, and density $\rho = 3210.05$ kg/m^3. As depicted in Fig. 7c that the dynamic response of the transverse deflection of the center of a square plate is in good agreement with the response obtained from COMSOL.

The first natural frequency of the plate with different thicknesses and boundary conditions is also compared to the analytical and literature results [44]. Two thickness to length ratios (h/a) is considered i.e., 0.01 and 0.1. CCCC stands for all sides clamped and SSSS stands for all sides subjected to simply supported conditions. The normalized natural frequency is reported in Table 4, where $\overline{\omega} = \omega a \sqrt{\frac{\rho}{G}}$, a is the side of the plate and G is the shear modulus.

5.4. Homogenized properties of photostrictive composites

Effective properties of particulate and fiber composites are determined numerically by implementing finite element method as discussed in Section 2.3. The matrix is PTB7-Th and inclusion material is PMN-35PT, their material properties are mentioned in Table 5. In the

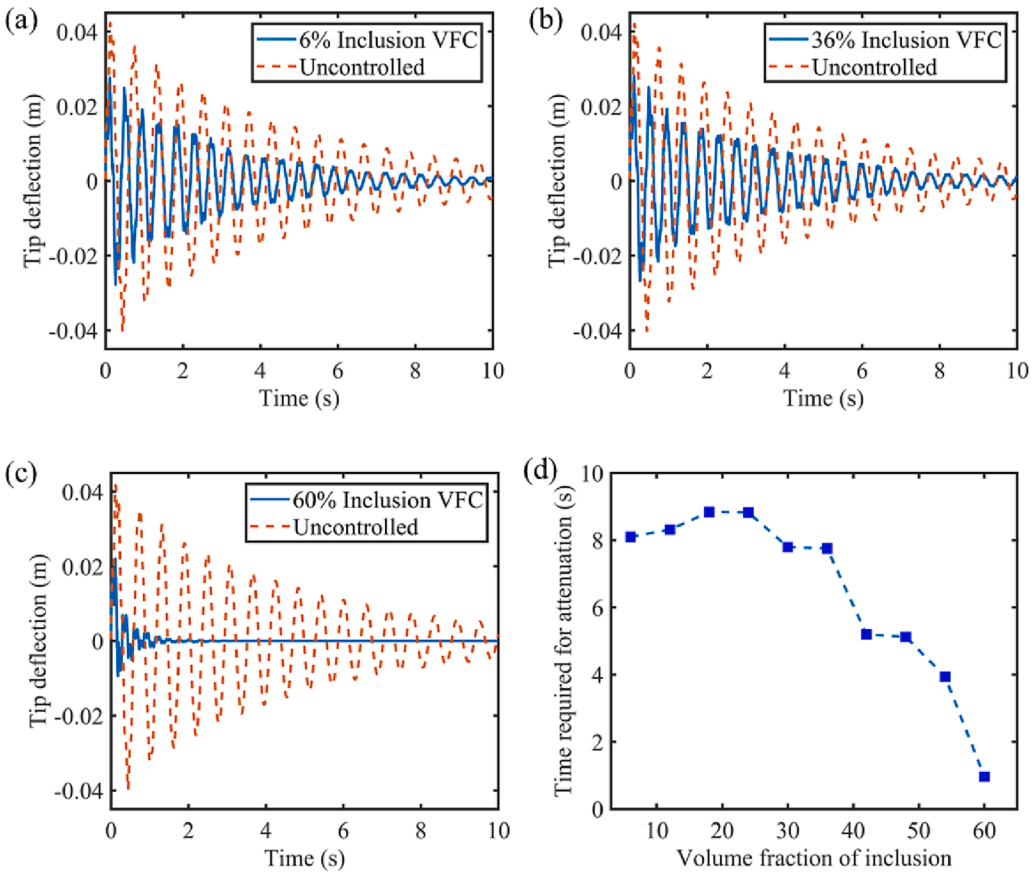

Fig. 11. Vibration response of velocity feedback-controlled cantilever structure when bonded with photostrictive fiber composite (with fiber arranged in square manner) of inclusion's volume fraction (a) 6 %, (b) 36 %, (c) 60 % and (d) time required to achieve approximately 95 % vibration attenuation.

particulate composite, the volume fraction of the spherical inclusions varies from 6 % to 30 %, and in the fiber composite, the volume fraction of the fiber varies from 6 % to 60 %. Two kinds of fiber arrangement are considered i.e., square and hexagonal arrangements of the fiber as shown in Fig. 2b and 2c. The values of evaluated effective elastic stiffness for particle composite and fiber composite are depicted in Fig. 1S and 2S, respectively in supplementary material. As a piezoelectric ceramic's volume fraction is increasing in the non-piezoelectric polymer matrix, hence the piezoelectric electromechanical coupling coefficient should increase. The aforementioned statement stands true for all the composites studied in the current study, which can also be observed in Fig. 8a and 9a. As it is well known that ceramics have a higher dielectric constant than polymer, therefore with an increase in ceramic volume fraction in composites, the effective dielectric constant increases, which can also be seen in Fig. 8b and 9b. Whereas the effective thermal expansion decreases with an increase in PMN35PT ceramic volume fraction in a photovoltaic polymer (see Fig. 8c and 9c). A dynamic numerical method is used to evaluate the effective pyroelectric coefficient. A small harmonic temperature simulation is provided to the RVE of the composites [34]. The effective pyroelectric coefficient has shown an increasing trend for all the composites studied in the current study, as shown in Fig. 8d and 9d. The increase in effective properties of composites such as piezoelectric coupling coefficient, dielectric constant, and pyroelectric coefficient will help to attain high photostriction. All the evaluated effective properties for particle and fiber composites are mentioned in Tables 1S and 2S respectively, in supplementary material.

5.5. Performance of photostrictive composites with velocity feedback control

This section discusses the active vibration control response of a cantilever structure of dimensions $1 \times 0.03 \times 0.002$ m. The cantilever structure is discretized with 10×1 elements. This cantilever structure has two patches of photostrictive material at a distance of 0.2 m from the fixed end on the top and bottom surface as shown in Fig. 1. These photostrictive actuators are subjected to light irradiation simultaneously to attenuate the vibration in the least possible time. The host structure is made up of mild steel, which has Young's Modulus $E = 2.1 \times 10^{11}$ N/m^2 and density $\rho = 7.8 \times 10^3$ kg/m^3. The photostrictive patch is considered to be particle composite or fiber composite. The dimensions of the photostrictive patch are $0.2 \times 0.03 \times 0.0003$ m. The time increment value used for Equations (2) and (3) is 1×10^{-3}. Firstly, the structure is controlled with a velocity feedback algorithm to investigate the effect of different kinds and inclusion volumes of photostrictive composites. The properties of photostrictive composite actuators are evaluated before the active vibration control simulation as discussed in Section 5.3. For evaluating the effect of spherical particle's volume fraction in velocity feedback vibration control response, the value of gain is considered as 5.05×10^7 (see Equation (44) which is constant along with the boundary condition for all the particulate composite (i.e., particulate composite with inclusion's volume fraction of 6 % to 30 %). The cantilever structure is disturbed with an impulse force of 10 N at the free end. It can be observed from Fig. 10a to 10c, that with the increase in inclusion's volume fraction in particulate composite the active vibration control response is getting better i.e., faster attenuation of vibrations is obtained. Fig. 10d shows the settling time to achieve approximately 95 % vibration attenuation for particulate composite with increasing inclusion's volume fraction. The uncontrolled response represents the damped response of the structure.

A similar trend of active vibration control of cantilever structure when bonded with fiber composite of both kinds (i.e., fiber arranged in

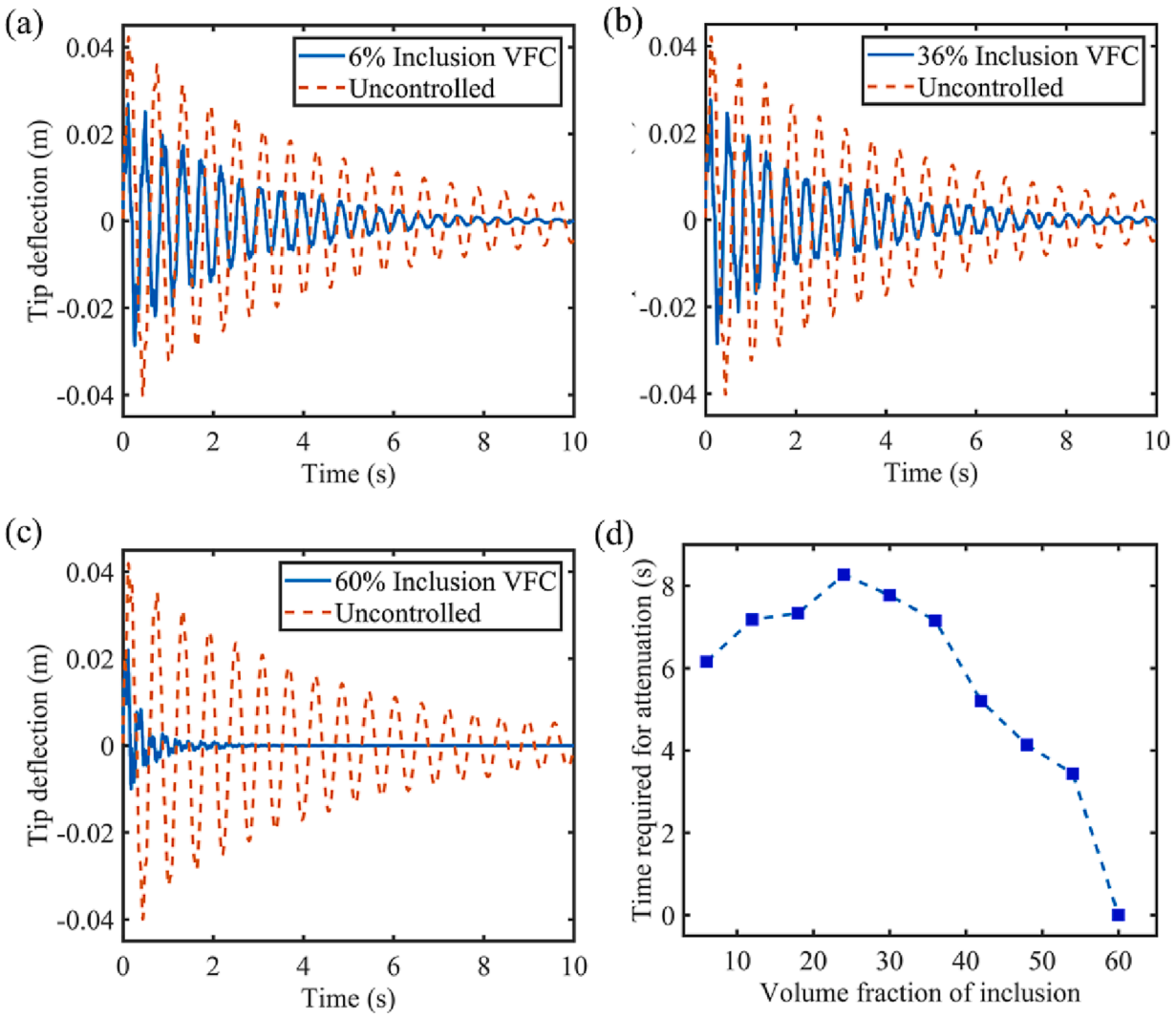

Fig. 12. Vibration response of velocity feedback-controlled cantilever structure when bonded with photostrictive fiber composite (with fiber arranged in hexagonal manner) of inclusion's volume fraction (a) 6 %, (b) 36 %, (c) 60 % and (d) time required to achieve approximately 95 % vibration attenuation.

square and hexagonal manner) was observed. Fig. 11(a)-(c) depict the vibration response of the cantilever structure bonded with fiber composite having fibers arranged in a square manner, and inclusion's volume fraction increases from 6 % to 60 %, respectively. While Fig. 12(a)-(c) depict the vibration response of the cantilever structure bonded with fiber composite having fibers arranged in hexagonal manner, and inclusion's volume fraction increases from 6 % to 60 %, respectively. Observing Fig. 11d and 12d, it is evident that till the inclusion's volume fraction of 25 %, the improvement in piezoelectric properties are less dominant in comparison to the increase in mechanical stiffness, however, after 25 % inclusion's volume fraction piezoelectric properties dominate the stiffness and hence better control response is obtained. The value of gain is considered as 3.47×10^7 and 3.60×10^7 (see Equation (44) for all the cases of fiber composites with fiber arranged in square and hexagonal manner, respectively. Fig. 11d and 12d show the settling time to achieve approximately 95 % vibration attenuation for fiber composite having fiber arranged in a square and hexagonal manner, respectively. The settling time first increases and then decreases with increasing volume fraction, this statement is true for both kinds of fiber composite. The variation of light intensity irradiated over upper and lower photostrictive actuator with time, while controlling cantilever structure with velocity feedback control is shown in Fig. 13. The variation of light intensity is plotted only for the composite with maximum inclusion's volume fraction i.e., 30 % and 60 % in particulate and fiber composite respectively. It can be observed from Fig. 13 that the value of light intensity gradually drops to zero, as the vibrations attenuate. Fig. 13a, 13c, and 13e represent the variation of light intensity irradiation over the upper photostrictive particulate composite, fiber composite with fiber arranged in a square and hexagonal arrangement. Whereas, Fig. 13b, 13d, and 13f represent the variation of light intensity irradiation over the lower photostrictive particulate composite, fiber composite with fiber arranged in a square and hexagonal arrangement.

5.6. *Performance of photostrictive composites with fuzzy logic control*

This section discusses the active vibration response of the cantilever structure equipped with photostrictive composite actuator patch on top and bottom surfaces of the host structure. The properties and dimension of the host structure and photostrictive actuator are the same for this analysis too, as discussed in Section 5.4. For the analysis with particulate photostrictive composites, the value of I_{max} is considered to be 1.5×10^7 (see Equation (46). Fig. 14a, 14b, and 14c represent the vibration response of the cantilever structure when equipped with an upper and lower photostrictive composite actuator of different inclusion's volume fractions i.e., 6 %, 18 %, and 30 % respectively. It can be observed from Fig. 14a to 14c that the controlled response is somewhat similar for different particulate photostrictive composites and there is also a very small difference in time required to attain 95 % vibration attenuation.

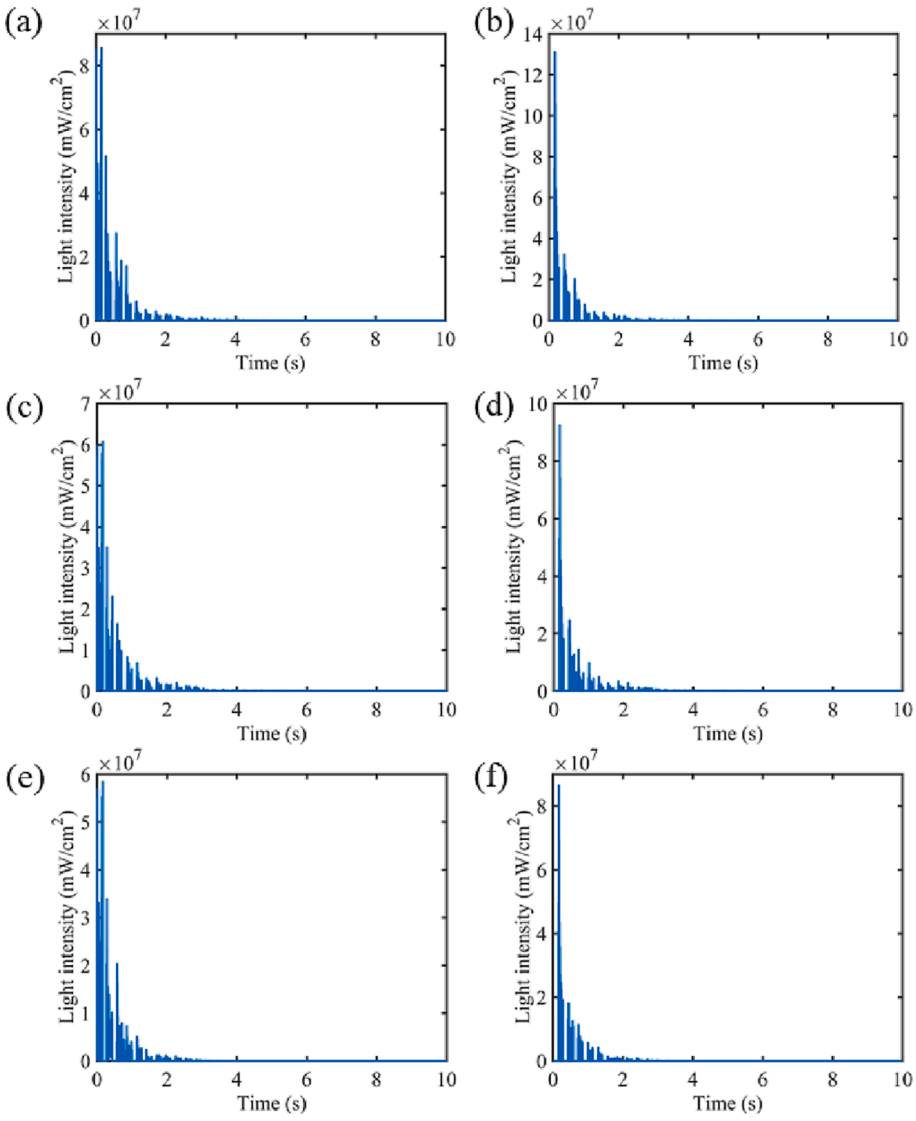

Fig. 13. Variation of light intensity with time at (a), (c), (e)upper and (b), (d), (f) lower photostrictive composite (i.e., particulate composite with 30 % inclusion, fiber composite with fiber arrange in square and hexagonal manner with 60 % inclusion) when controlled with velocity feedback controller.

This has happened due to a self-tunable fuzzy logic controller. Fig. 14d shows the time required to attain 95 % vibration attenuation for particulate photostrictive composite with different inclusion volume fractions.

A similar trend for active vibration control of cantilever structure bonded with fiber photostrictive composite was obtained. For the analysis with fiber photostrictive composites (i.e., fiber aligned in a square and hexagonal manner), the value of I_{max} is considered to be 8×10^6 and 1×10^7, respectively. Small enhancement in response to vibration control is achieved with an increase in inclusion's volume fraction. Owing to the fuzzy logic control tuning capability, the vibration response of fiber composite with different volume fractions is approximately the same. It can be seen from Fig. 15, where Fig. 15a, 15b, and 15c represent the controlled and uncontrolled vibration response of the cantilever structure bonded with fiber composite having fiber aligned in a square manner Fig. 15d and 16d show the time required to achieve 95 % of the vibration attenuation for the inclusions volume fraction of fiber arranged in a square and hexagonal manner varies from 6 % to 60 %. Whereas, Fig. 16a, 16b, and 16c represent the controlled and uncontrolled vibration response of the cantilever structure bonded with fiber composite having fiber aligned in hexagonal manner. No significant difference in settling time is obtained as a function of inclusion's volume fraction for both kind of fiber composites, while the persistent small vibrations are eliminated as the inclusion's volume fraction is increased. The variation of light intensity irradiated over upper and lower photostrictive actuator with time, while controlling cantilever structure with fuzzy logic control is shown in Fig. 17. The variation of light intensity is plotted only for the composite with maximum inclusion's volume fraction i.e., 30 % and 60 % in particulate and fiber composite respectively. It can be observed from Fig. 17 that the value of light intensity suddenly drops to zero, as the vibrations attenuate because of the control algorithm discussed in Section 4.2. Fig. 17a, 17c, and 17e represent the variation of light intensity irradiation over the upper photostrictive particulate composite, fiber composite with fiber arranged in square and hexagonal arrangements. Whereas, Fig. 17b, 17d, and 17f represent the variation of light intensity irradiation over the lower photostrictive particulate composite, fiber composite with fiber arranged in square and hexagonal arrangements.

5.7. Stability analysis

A system is considered stable if the achieved output is finite for every bounded input, also known as BIBO stability. As shown in Figs. 10, 11, 12, 14, 15, and 16 the displacement response approaches zero with time.

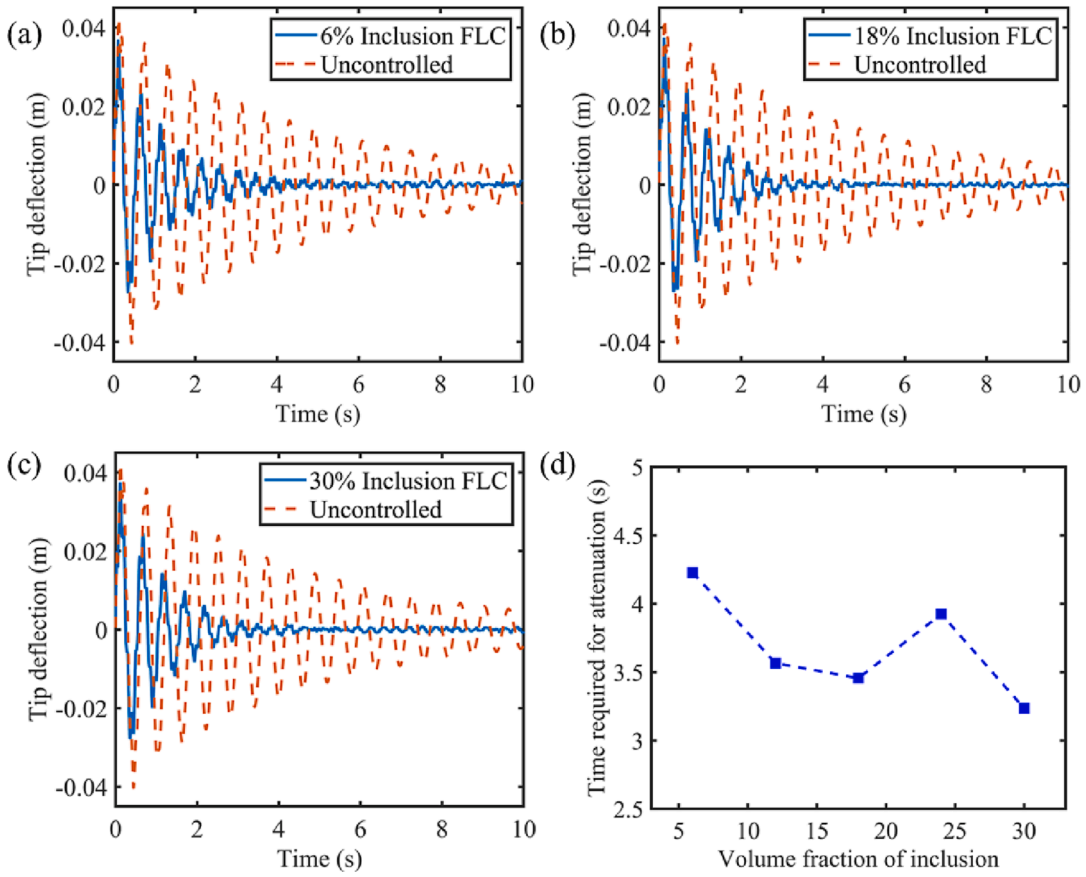

Fig. 14. Vibration response of fuzzy logic-controlled cantilever structure when bonded with photostrictive particulate composite of inclusion's volume fraction (a) 6 %, (b) 18 %, (c) 30 %, and (d) time required to achieve approximately 95 % vibration attenuation.

The phase diagrams of the controlled response of cantilever structure with both velocity feedback and the fuzzy logic controller are shown in Fig. 18. Fig. 18a, 18b, and 18c demonstrate the velocity and displacement response of cantilever structure controlled with velocity feedback and equipped with particulate composite with 30 % inclusions volume fraction, 60 % volume fraction of fiber composite with a square and hexagonal arrangement. Whereas Fig. 18d, 18e, and 18f demonstrate the velocity and displacement response of cantilever structure controlled with fuzzy logic and equipped with particulate composite with 30 % inclusions volume fraction, 60 % volume fraction of fiber composite with a square and hexagonal arrangement. The system shows asymptotically stable nature for every case and stable for the structure bonded with particulate composite and controlled with a fuzzy logic controller.

5.8. Effect of light switching function

The light switching function (see Section 4.2) helps to eliminate the small consistent vibrations at the later stage, and smooth out the control discontinuity. Fig. 19 demonstrates the uncontrolled and controlled response of active vibration control of cantilever structure with and without employing light switching function. Fig. 19a, 19b, and 19c are the vibration response of cantilever structure equipped with particulate composite, and fiber composite with fiber aligned in square and hexagonal arrangements, respectively. It can easily be observed from Fig. 19a, 19b, and 19c that the light switching function successfully eliminates the small vibration at the end i.e., chattering.

5.9. Comparison of velocity feedback and fuzzy logic control response

To compare the control response of the cantilever structure, it is considered that the intensity of the light to be irradiated over photostrictive composite will be constant, along with the boundary conditions and type of photostrictive composite, while controlling it with velocity feedback and fuzzy logic control. Fig. 20a, 20b, and 20c show the uncontrolled and controlled response of the cantilever structure with velocity feedback control (VFC) and fuzzy logic control (FLC). The max light intensity applied on particulate (30 % inclusion's volume fraction) and fiber composite (60 % inclusion's volume fraction) with fiber aligned in square and hexagonal fashion is 1.26×10^7, 6.68×10^6 and 8.35×10^6, respectively.

From Fig. 20, it is prudent to say that with less light intensity faster vibration attenuation can be achieved by employing fuzzy logic control.

5.10. Control merit

To compare the controlling capability of the different photostrictive composites, a parameter called control merit is defined in this study. The control merits (CM) can be defined as,

$$CM_1 = \frac{1}{t_a I_{max}}, CM_2 = \frac{1}{t_a I_{max} \rho} \tag{49}$$

where t_a is the time required to attain 95 % vibration attenuation, I_{max} is the maximum light intensity, and ρ is the density of the composite material.

Fig. 21a and 21b depicts the values of CM_1 and CM_2, respectively for different photostrictive composite materials. Fig. 21a shows that fiber composite with fiber aligned in a square fashion (SFC) shows the

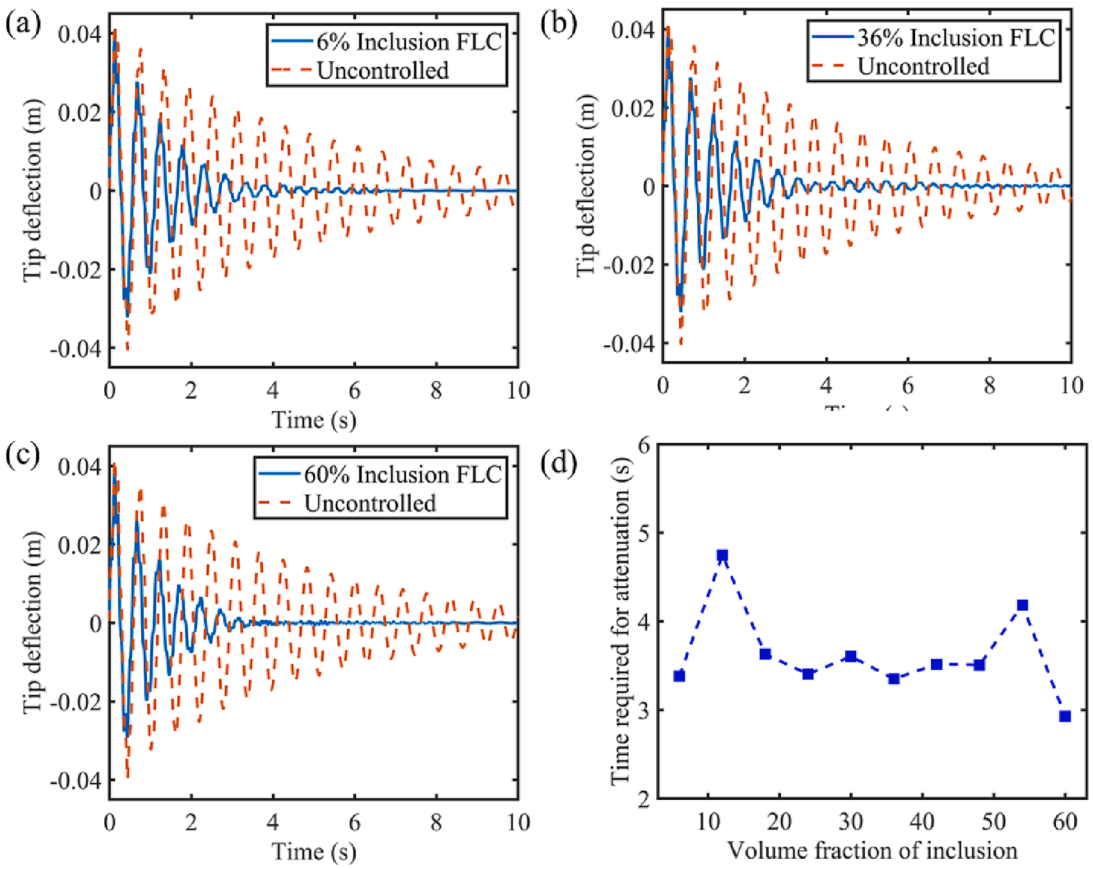

Fig. 15. Vibration response of fuzzy logic-controlled cantilever structure when bonded with photostrictive fiber composite (with fiber arranged in square manner) of inclusion's volume fraction (a) 6 %, (b) 36 %, (c) 60 % and (d) time required to achieve approximately 95 % vibration attenuation.

maximum value of control merit (CM_1), in comparison to particulate composite (PC) and fiber composite with fiber aligned in hexagonal fashion (HFC). The inclusion's volume fraction is 30 %, 60 %, and 60 % for PC, SFC, and HFC, respectively. The green and blue color bar in Fig. 21 refers to the control merit value when the structure is controlled with velocity feedback (VFC) and fuzzy logic controller (FLC), respectively. From Fig. 21a, it is prudent to say that SFC gives the best performance to attenuate the 95 % vibration in the least time with the fuzzy logic controller. However, if these control merit values are divided by density, then PC shows to be the best performer in vibration control with photostrictive composite and fuzzy logic control, as shown in Fig. 21b. When the desired quality is lightweight, then PC can be selected, otherwise, SFC would be the choice for wireless vibration control.

6. Conclusions

The current study presented a finite element formulation to wirelessly control the cantilever host structure bonded with photostrictive composite actuators using visible light irradiation. Overall Multiphysics properties (i.e., effective mechanical, electrical, thermal, and pyroelectric properties) of particulate and fiber photostrictive composites are investigated employing finite element-based numerical simulations. The present finite element formulation is validated with available literature for static, dynamic, and modal analysis. The current study comes up with the following conclusions:

(1) Present work opens up a new avenue to solve the issue of fewer choices of photostrictive material with high electromechanical coupling coefficients and which can also interact with a wider range of the light spectrum.
(2) Active vibration control response of cantilever structure shows that with an increase in volume fraction of piezoelectric ceramic in photovoltaic polymer, faster vibration attenuation was achieved. This statement holds good for both particulate and fiber composite.
(3) The fuzzy logic control algorithm dominates the effect of an increase in piezoelectric inclusion, as the time required to control even with a photostrictive composite with higher piezoelectric inclusion remains moreover same.
(4) A fuzzy logic controller performs well in comparison to conventional velocity feedback control, as it requires less light intensity to achieve faster vibration attenuation when all the geometric, material, and boundary conditions were kept constant.
(5) The light switching function helps to remove the small persisting vibrations at the later stage, it helps to improve the stability of the system.
(6) It is found that particulate composites are the better choice for lightweight structures and fiber composites are better if there is no weight constraint.

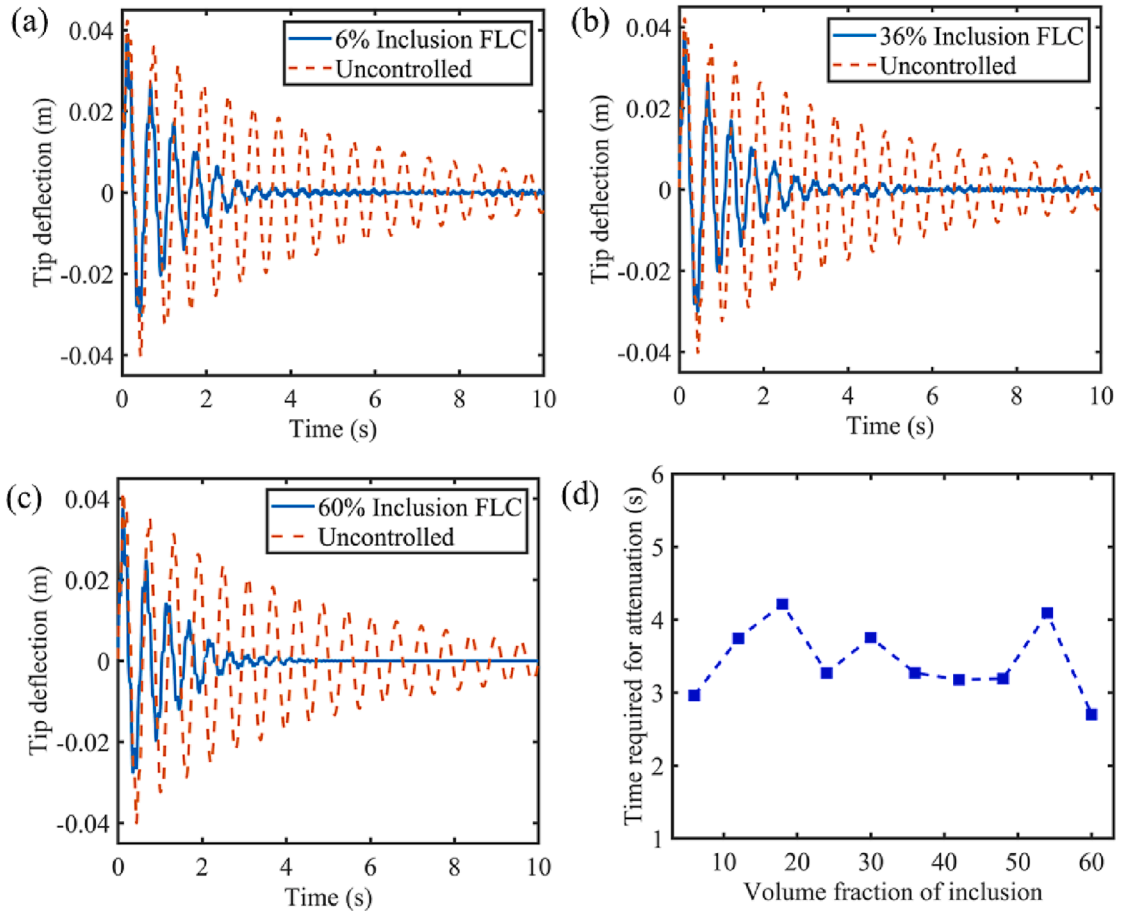

Fig. 16. Vibration response of fuzzy logic-controlled cantilever structure when bonded with photostrictive fiber composite (with fiber arranged in hexagonal manner) of inclusion's volume fraction (a) 6 %, (b) 36 %, (c) 60 % and (d) time required to achieve approximately 95 % vibration attenuation.

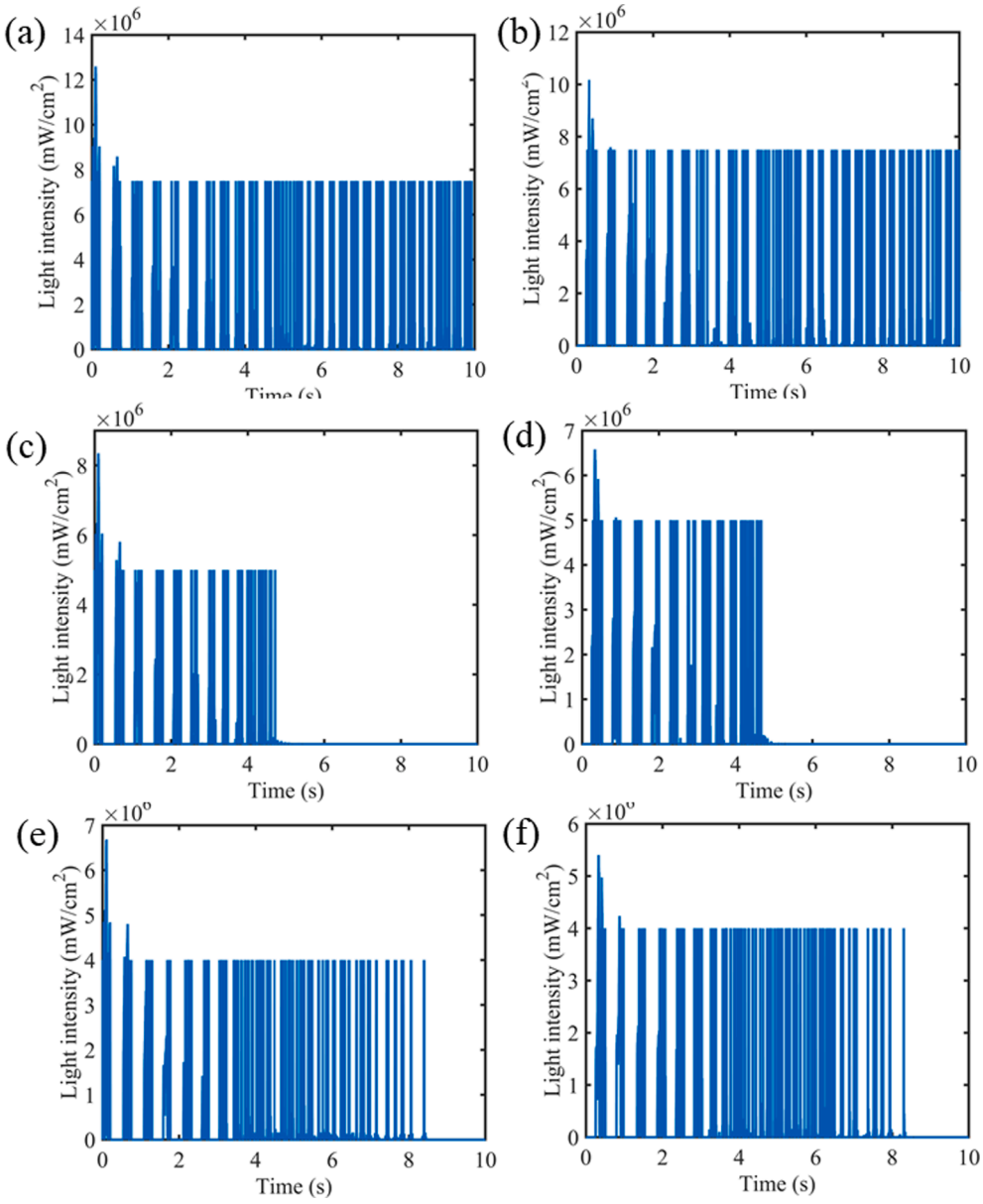

Fig. 17. Variation of light intensity with time at (a), (c), (e)upper and (b), (d), (f) lower photostrictive composite (i.e., particulate composite with 30 % inclusion, fiber composite with fiber arrange in square and hexagonal manner with 60 % inclusion) when controlled with fuzzy logic controller.

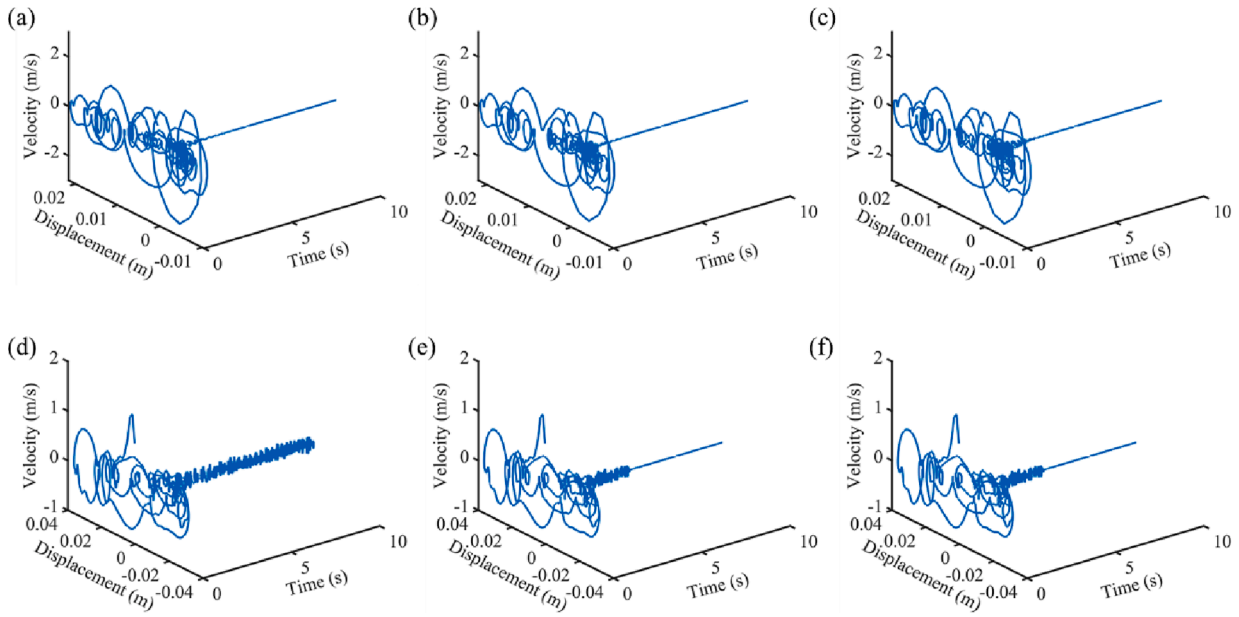

Fig. 18. Stability analysis of cantilever structure, which is equipped with (a), (d) particulate composite, (b), (e) fiber composite with fiber aligned in a square manner, (c), and (f) fiber composite with fiber aligned in a hexagonal manner, when controlled with velocity feedback and fuzzy logic controller respectively.

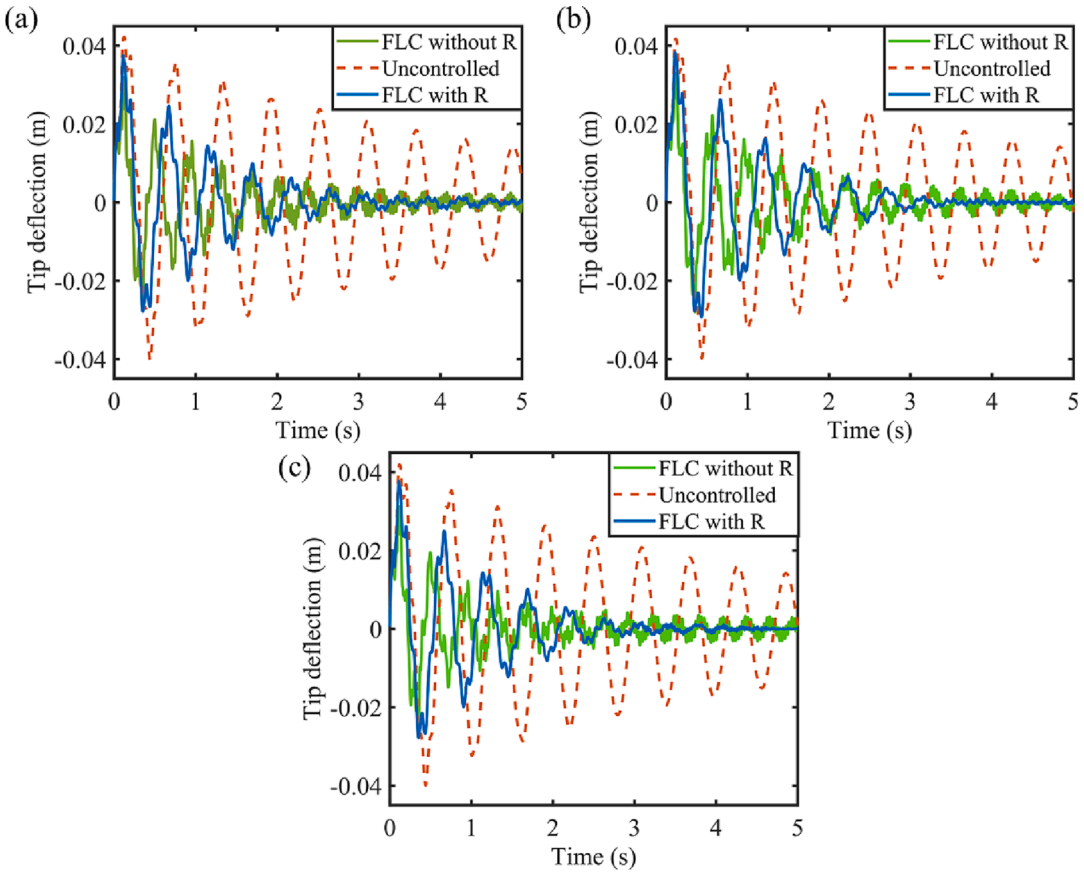

Fig. 19. Comparison of a fuzzy logic-controlled cantilever beam with and without function R, when equipped with (a) particulate composite, (b) fiber composite with fiber aligned in a square manner, and (d) fiber composite with fiber aligned in a hexagonal manner.

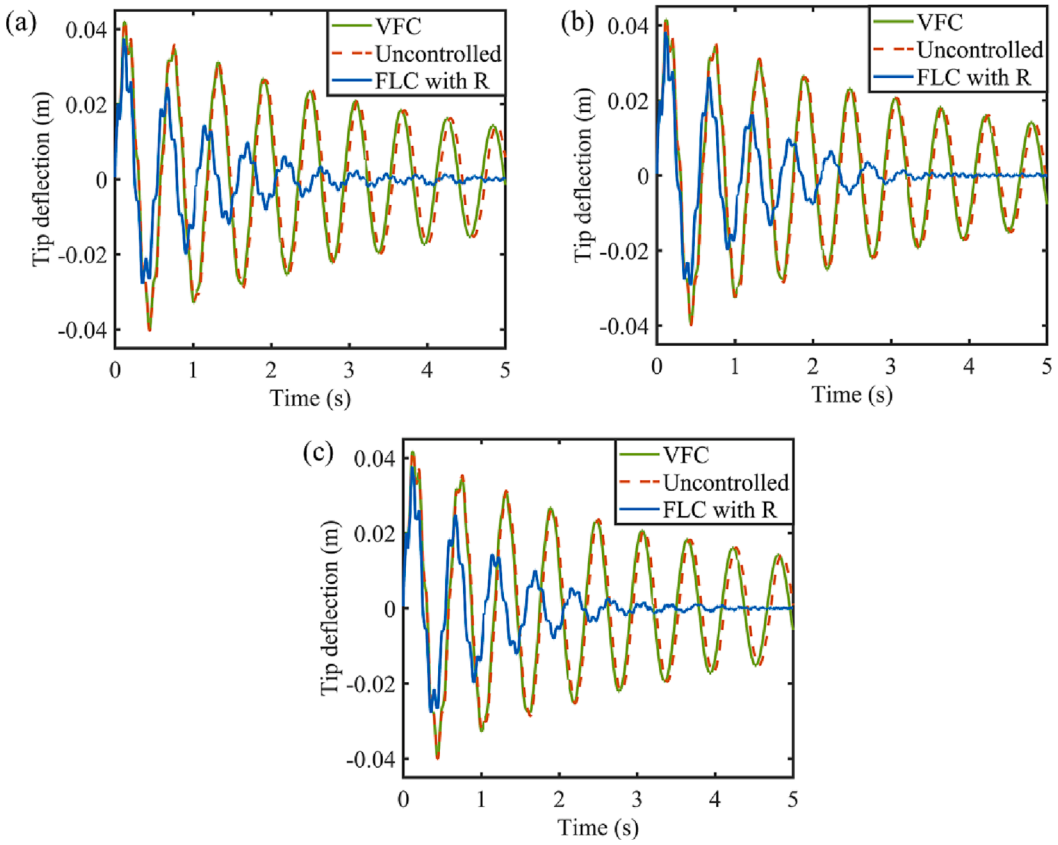

Fig. 20. Comparison of velocity feedback and fuzzy logic controller response, when cantilever structure is equipped with (a) particulate composite, (b) fiber composite with fiber aligned in a square manner, and (d) fiber composite with fiber aligned in a hexagonal manner.

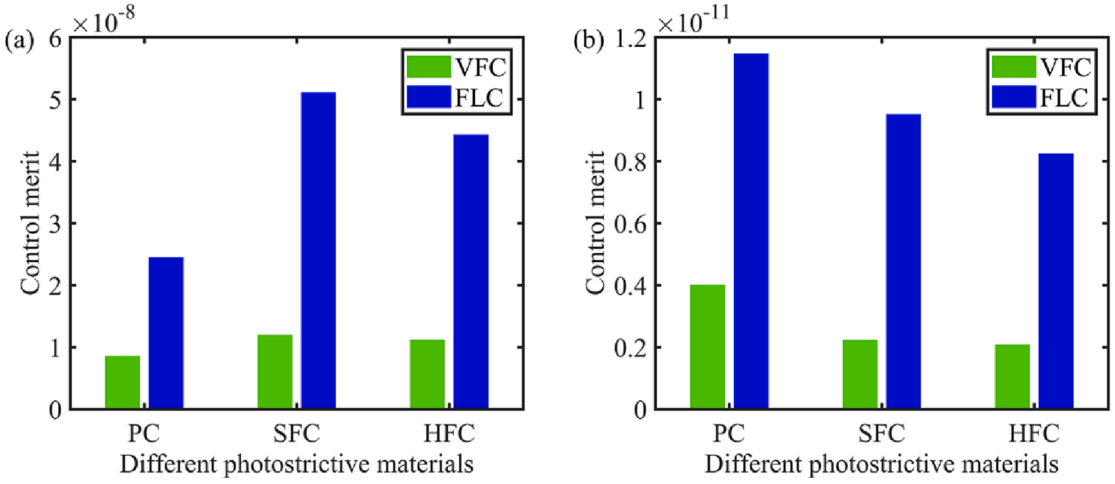

Fig. 21. Comparison of different photostrictive composite material using control merit (a) CM_1 and (b) CM_2 values.

Data Availability

All the data required to reproduce the finding of current work has been mentioned in this full length article.

Declaration of Competing Interest

The authors declare that they have no known competing financial interests or personal relationships that could have appeared to influence the work reported in this paper.

Data availability

All the data required to reproduce the finding of current work has been mentioned in this full length article.

Appendix A

$$H_i = t_{ok_i} + \frac{\zeta_k}{2} t_{k_i}, \tag{A.1}$$

where t_{ok_i} refers to the distance between the k^{th} layer and neutral layer, t_{k_i} is the thickness of the kth layer at any node i.

$$[B]_i = \begin{bmatrix} \frac{\partial N_i}{\partial x} & 0 & 0 & & \\ 0 & \frac{\partial N_i}{\partial y} & 0 & & \\ 0 & 0 & \frac{\partial N_i}{\partial z} & -l_{2i}g_{xi} & l_{1i}g_{xi} \\ & & & -m_{2i}g_{yi} & m_{1i}g_{yi} \\ & & & -n_{2i}g_{zi} & n_{1i}g_{zi} \\ \frac{\partial N_i}{\partial y} & \frac{\partial N_i}{\partial x} & 0 & -\left(l_{2i}g_{yi} + m_{2i}g_{xi}\right) & \left(l_{1i}g_{yi} + m_{1i}g_{xi}\right) \\ 0 & \frac{\partial N_i}{\partial z} & \frac{\partial N_i}{\partial y} & -\left(m_{2i}g_{zi} + n_{2i}g_{yi}\right) & \left(m_{1i}g_{zi} + n_{1i}g_{yi}\right) \\ \frac{\partial N_i}{\partial z} & 0 & \frac{\partial N_i}{\partial x} & -\left(n_{2i}g_{xi} + l_{2i}g_{zi}\right) & \left(n_{1i}g_{xi} + l_{1i}g_{zi}\right) \end{bmatrix} \{q\}_i = \begin{Bmatrix} u_{oi} \\ v_{oi} \\ w_{oi} \\ \alpha_i \\ \beta_i \end{Bmatrix} \tag{A.2}$$

where

$$g_{xi} = N_i\frac{\partial H_i}{\partial x} + H_i\frac{\partial N_i}{\partial x}, g_{yi} = N_i\frac{\partial H_i}{\partial y} + H_i\frac{\partial N_i}{\partial y}, g_{zi} = N_i\frac{\partial H_i}{\partial z} + H_i\frac{\partial N_i}{\partial z} \tag{A.3}$$

$$\begin{Bmatrix} \sigma_{11} \\ \sigma_{22} \\ \sigma_{12} \\ \sigma_{13} \\ \sigma_{23} \end{Bmatrix}_e = \begin{bmatrix} Q_{11}^{'} & Q_{12}^{'} & 0 & 0 & 0 \\ Q_{21}^{'} & Q_{22}^{'} & 0 & 0 & 0 \\ 0 & 0 & Q_{66}^{'} & 0 & 0 \\ 0 & 0 & 0 & Q_{55}^{'} & 0 \\ 0 & 0 & 0 & 0 & Q_{44}^{'} \end{bmatrix} \tag{A.4}$$

$$Q_{11}^{'} = \frac{Q_{11}Q_{33} - (Q_{13})^2}{Q_{33}}, Q_{12}^{'} = \frac{Q_{12}Q_{33} - Q_{13}Q_{23}}{Q_{33}}, Q_{22}^{'} = \frac{Q_{22}Q_{33} - (Q_{23})^2}{Q_{33}}, Q_{66}^{'} = Q_{66}, Q_{55}^{'} = Q_{55}, Q_{44}^{'} = Q_{44}. \tag{A.5}$$

$$\{B_\phi\}_e = \frac{1}{t_{pk}} \begin{Bmatrix} l_3 \\ m_3 \\ n_3 \end{Bmatrix} \tag{A.6}$$

where t_{pk} is the thickness of the k^{th} photostrictive layer.

$$\{B_\theta\}_e = \frac{1}{t_{P_k}} \begin{Bmatrix} l_3 \\ m_3 \\ n_3 \end{Bmatrix}. \tag{A.7}$$

$$[\overline{e}]_k = [T_v]^T[e]_k[T_o]_k, [\overline{b}]_k = [T_v]^T[b]_k[T_v], \{\overline{p}\}_k = [T_v]^T\{p\}_k, \tag{A.8}$$

$$[\overline{Q}]_k = [T_\varepsilon]^T[T_o]^T[Q]_k[T_o][T_\varepsilon], \{\overline{\lambda}\}_k = [T_\varepsilon]^T[T_o]^T\{\lambda\}_k. \tag{A.9}$$

$$[T_0] = \begin{bmatrix} c^2 & s^2 & 0 & cs & 0 & 0 \\ s^2 & c^2 & 0 & -cs & 0 & 0 \\ 0 & 0 & 1 & 0 & 0 & 0 \\ -2cs & 2cs & 0 & c^2 - s^2 & 0 & 0 \\ 0 & 0 & 0 & 0 & c & s \\ 0 & 0 & 0 & 0 & -s & c \end{bmatrix} \tag{A.10}$$

$$[T_\varepsilon] = \begin{bmatrix} l_1^2 & m_1^2 & n_1^2 & l_1m_1 & m_1n_1 & n_1l_1 \\ l_2^2 & m_2^2 & n_2^2 & l_2m_2 & m_2n_2 & n_2l_2 \\ l_3^2 & m_3^2 & n_3^2 & l_3m_3 & m_3n_3 & n_3l_3 \\ 2l_1\,l_2 & 2m_1\,m_2 & 2n_1\,n_2 & (l_1m_2+l_2m_1) & (m_1n_2+m_2n_1) & (n_1l_2+n_2l_1) \\ 2l_2\,l_3 & 2m_2\,m_3 & 2n_2\,n_3 & (l_2m_3+l_3m_2) & (m_2n_3+m_3n_2) & (n_2l_3+n_3l_2) \\ 2l_3\,l_1 & 2m_3\,m_1 & 2n_3\,n_1 & (l_3m_1+l_1m_3) & (m_3n_1+m_1n_3) & (n_3l_1+n_1l_3) \end{bmatrix} \tag{A.11}$$

$$[T_v] = \begin{bmatrix} l_1 & m_1 & n_1 \\ l_2 & m_2 & n_2 \\ l_3 & m_3 & n_3 \end{bmatrix} \tag{A.12}$$

$$[K_{uu}]_e = \sum_{k=1}^{nl} \int_V [B]_e^T [\overline{Q}]_k [B]_e dV \tag{A.13}$$

$$\left[K_{u\phi}\right]_e = \sum_{k=1}^{npl} \int_V [B]_e^T [\overline{e}]_k \left[B_\phi\right]_e dV \tag{A.14}$$

$$[K_{u\theta}]_e = \sum_{k=1}^{npl} \int_V [B]_e^T [\overline{\lambda}]_k dV \tag{A.15}$$

where *nl* refers to the total number of layers, and *npl* represents total number of photostrictive layer.

$$\left[K_{\phi u}\right]_e = \left[K_{u\phi}\right]_e^T \tag{A.16}$$

$$\left[K_{\phi\phi}\right]_e = \sum_{k=1}^{npl} \int_V \left[B_\phi\right]_e^T [\overline{b}]_k \left[B_\phi\right]_e dV \tag{A.17}$$

$$\left[K_{\phi\theta}\right]_e = \sum_{k=1}^{npl} \int_V \left[B_\phi\right]_e^T [\overline{p}]_k dV \tag{A.18}$$

$$[H_{\theta\theta}] = \sum_{k=1}^{npl} \int_V [\alpha_v] dV \tag{A.19}$$

$$[m_{uu}]_e = \sum_{k=14}^{nl} \int_V \rho_k [T_\theta]_e^t [N_{\bar{u}}]_e^t [N_{\bar{u}}]_e [T_\theta]_e dV \tag{A.20}$$

$$[C_{uu}] = \alpha[M_{uu}] + \beta[K_{uu}] \tag{A.21}$$

where α and β are the Rayleigh's coefficients.

Appendix B. Supplementary material

Supplementary data to this article can be found online at https://doi.org/10.1016/j.compstruct.2023.116919.

References

[1] Crawley EF. Intelligent structures for aerospace: A technology overview and assessment. AIAA J 1994;32:1689–99. https://doi.org/10.2514/3.12161.

[2] Tzou HS, Anderson GL. Intelligent structural systems, vol. 13. Springer Science & Business Media; 2013.

[3] Zheng S, Wang X, Chen W. The formulation of a refined hybrid enhanced assumed strain solid shell element and its application to model smart structures containing distributed piezoelectric sensors/actuators. Smart Mater Struct 2004;13:N43.

[4] Sharma S, Kumar R, Talha M, Vaish R. Design of spatially varying electrical poling for enhanced piezoelectricity in Pb (Mg1/3Nb2/3) O3–0.35 PbTiO3. Int J Mech Mater Des 2021;17:99–118.

[5] Sharma S, Kumar A, Kumar R, Talha M, Vaish R. Active vibration control of smart structure using poling tuned piezoelectric material. J Intell Mater Syst Struct 2020; 31:1298–313. https://doi.org/10.1177/1045389X20917456.

[6] Uchino K, Aizawa M, Nomura LS. Photostrictive effect in (Pb, La)(Zr, Ti) O3. Ferroelectrics 1985;64:199–208.

[7] Bai Y, Jantunen H, Juuti J. Energy harvesting research: the road from single source to multisource. Adv Mater 2018;30:1707271.

[8] Paillard C, Bai X, Infante IC, Guennou M, Geneste G, Alexe M, et al. Photovoltaics with ferroelectrics: Current status and beyond. Adv Mater 2016;28:5153–68.

[9] Mamoun S, Merad AE, Guilbert L. Energy band gap and optical properties of lithium niobate from ab initio calculations. Comput Mater Sci 2013;79:125–31.

[10] Bai Y, Siponkoski T, Peräntie J, Jantunen H, Juuti J. Ferroelectric, pyroelectric, and piezoelectric properties of a photovoltaic perovskite oxide. Appl Phys Lett 2017; 110:63903.

[11] Zhong H, Xiao H, Jiao N, Guo Y. Boosting piezoelectric response of KNN-based ceramics with strong visible-light absorption. J Am Ceram Soc 2019;102:6422–6.

[12] Xiao H, Luo C, Huangfu G, Guo Y. Boosting the photocatalytic ability of bandgap engineered (Na0. 5Bi0. 5) TiO3–BaTiO3 by N-Ni codoping. J Phys Chem C 2020; 124:11810–8.

[13] Tzou HS, Chou CS. Nonlinear opto-electromechanics and photodeformation of optical actuators. Smart Mater Struct 1996;5:230.

[14] Liu B, Tzou HS. Distributed photostrictive actuation and opto-piezothermoelasticity applied to vibration control of plates 1998.

[15] Shih H-R, Smith R, Tzou H-S. Photonic control of cylindrical shells with electro-optic photostrictive actuators. Aiaa J 2004;42:341–7.

[16] Shih H-R, Tzou H-S, Saypuri M. Structural vibration control using spatially configured opto-electromechanical actuators. J Sound Vib 2005;284:361–78.

[17] Wang XJ, Yue HH, Jiang J, Deng ZQ, Tzou HS. Wireless active vibration control of thin cylindrical shells laminated with photostrictive actuators. J Intell Mater Syst Struct 2011;22:337–51.

[18] Jiang J, Wang L, Yue H, Deng Z, Tzou H. Vibration control of cylindrical shells with a hybrid photovoltaic/piezoelectric actuation mechanism. Int J Appl Electromagn Mech 2014;46:917–26.
[19] Sun D, Tong L. Theoretical investigation on wireless vibration control of thin beams using photostrictive actuators. J Sound Vib 2008;312:182–94.
[20] He R, Zheng S. Independent modal variable structure fuzzy active vibration control of thin plates laminated with photostrictive actuators. Chinese J Aeronaut 2013;26:350–6.
[21] He RB, Zheng SJ, Wang HT. Independent modal variable structure fuzzy active vibration control of cylindrical thin shells laminated with photostrictive actuators. Shock Vib 2013;20:693–709.
[22] Sharma A, Kumar R, Vaish R, Chauhan VS. Active vibration control of space antenna reflector over wide temperature range. Compos Struct 2015;128:291–304.
[23] Sharma A, Kumar A, Susheel CK, Kumar R. Smart damping of functionally graded nanotube reinforced composite rectangular plates. Compos Struct 2016;155:29–44.
[24] Sharma A. Effect of porosity on active vibration control of smart structure using porous functionally graded piezoelectric material. Compos Struct 2022;280:114815.
[25] He R, Zheng S. Fuzzy neural network multi-modal vibration control of thin cylindrical shells laminated with photostrictive actuators. Int J Appl Electromagn Mech 2014;46:951–63.
[26] He R, Zheng S, Tong L. Multimodal vibration control of photo-electric laminated thin cylindrical shells via self-organizing fuzzy sliding mode control. J Vib Acoust 2016;138.
[27] Mancang JIA, Zheng S, Rongbo HE. Multi-mode optimal fuzzy active vibration control of composite beams laminated with photostrictive actuators. Chinese J Aeronaut 2019;32:1442–50.
[28] Singh D, Sharma S, Kumar R, Chauhan VS, Vaish R. Novel photostrictive 0–3 composites: A finite element analysis. Mech Adv Mater Struct 2021:1–12.
[29] Singh D, Sharma S, Kumar R, Chauhan VS, Vaish R. Photostrictive effect in 1–3 composites of photovoltaic and piezoelectric phases: A numerical study. J Intell Mater Syst Struct 2021. 1045389X211053050.
[30] Chan HLW, Unsworth J. Simple model for piezoelectric ceramic/polymer 1–3 composites used in ultrasonic transducer applications. IEEE Trans Ultrason Ferroelectr Freq Control 1989;36:434–41.
[31] Yu Li J, Dunn ML. Variational bounds for the effective moduli of heterogeneous piezoelectric solids. Philos Mag A 2001;81:903–26.
[32] Dunn ML, Wienecke HA. Inclusions and inhomogeneities in transversely isotropic piezoelectric solids. Int J Solids Struct 1997;34:3571–82.
[33] Berger H, Kari S, Gabbert U, Rodriguez-Ramos R, Bravo-Castillero J, Guinovart-Diaz R, et al. Unit cell models of piezoelectric fiber composites for numerical and analytical calculation of effective properties. Smart Mater Struct 2006;15:451.
[34] Magouh N, Dietze M, Bakhti H, Solterbeck C-H, Azrar L, Es-Souni M. Finite element analysis and EMA predictions of the dielectric and pyroelectric properties of 0–3 Pz59/PVDF-TrFE composites with experimental validation. Sensors Actuators A Phys 2020;310:112073.
[35] Shih H-R, Watkins J, Tzou H-S. Displacement control of a beam using photostrictive optical actuators. J Intell Mater Syst Struct 2005;16:355–63.
[36] Sharma M, Chauhan A, Vaish R, Chauhan VS. Pyroelectric materials for solar energy harvesting: A comparative study. Smart Mater Struct 2015:24. https://doi.org/10.1088/0964-1726/24/10/105013.
[37] Luo Q, Luo Z, Tong L. A variational principle and finite element formulation for multi-physics PLZT ceramics. Mech Res Commun 2011;38:198–202.
[38] Altay G, Dökmeci MC. The consistent Mindlin's thermopiezoelectric equations and the principle of virtual work. Mech Res Commun 2005;32:115–9.
[39] Suquet P. Elements of homogenization theory for inelastic solid mechanics. Zaoui A, Homogenization techniques for composite media: Sanchez-Palencia E; 1987.
[40] Berger H, Kari S, Gabbert U, Rodriguez-Ramos R, Guinovart R, Otero JA, et al. An analytical and numerical approach for calculating effective material coefficients of piezoelectric fiber composites. Int J Solids Struct 2005;42:5692–714. https://doi.org/10.1016/j.ijsolstr.2005.03.016.
[41] Wankhade RL, Bajoria KM. Free vibration and stability analysis of piezolaminated plates using the finite element method. Smart Mater Struct 2013;22:125040.
[42] Sharma A, Kumar R, Vaish R, Chauhan VS. Lead-free piezoelectric materials' performance in structural active vibration control. J Intell Mater Syst Struct 2014;25:1596–604.
[43] Kwak MK, Sciulli D. Fuzzy-logic based vibration suppression control experiments on active structures. J Sound Vib 1996;191:15–28.
[44] Ferreira AJM. MATLAB codes for finite element analysis. Springer; 2009.
[45] Levassort F, Pham Thi M, Hemery H, Marechal P, Tran-Huu-Hue LP, Lethiecq M. Piezoelectric textured ceramics: Effective properties and application to ultrasonic transducers. Ultrasonics 2006:44. https://doi.org/10.1016/j.ultras.2006.05.016.
[46] Huang W, Jiang Z, Fukuda K, Jiao X, McNeill CR, Yokota T, et al. Efficient and Mechanically Robust Ultraflexible Organic Solar Cells Based on Mixed Acceptors. Joule 2020;4:128–41. https://doi.org/10.1016/j.joule.2019.10.007.
[47] Lim LW, Aziz F, Muhammad FF, Supangat A, Sulaiman K. Electrical properties of Al/PTB7-Th/n-Si metal-polymer-semiconductor Schottky barrier diode. Synth Met 2016;221:169–75. https://doi.org/10.1016/j.synthmet.2016.08.018.
[48] Xu X, Chen J, Zhou J, Li B. Thermal Conductivity of Polymers and Their Nanocomposites. Adv Mater 2018;30:1–10. https://doi.org/10.1002/adma.201705544.
[49] Wongmaneerung R, Guo R, Bhalla A, Yimnirun R, Ananta S. Thermal expansion properties of PMN-PT ceramics. J Alloys Compd 2008;461:565–9. https://doi.org/10.1016/j.jallcom.2007.07.086.
[50] Weon HY, Jung JM, Choi SW, Kim YJ. Dielectric, piezoelectric and pyroelectric properties of Pb(Mg1/3Ta2/3)O3-PbTiO3-BaTiO3 system. Ferroelectrics 1994;158:253–8. https://doi.org/10.1080/00150199408216025.
[51] Caddeo C, Filippetti A, Bosin A, Videlot-Ackermann C, Ackermann J, Mattoni A. Theoretical insight on PTB7:PC71BM, PTB7-th:PC71BM and Si-PCPDTBT:PC71BM interactions governing blend nanoscale morphology for efficient solar cells. Nano Energy 2021;82:105708. https://doi.org/10.1016/j.nanoen.2020.105708.
[52] Wen J. Heat Capacities of Polymers. Phys Prop Polym Handb 2007:145–54. https://doi.org/10.1007/978-0-387-69002-5_9.
[53] Uršič H, Vrabelj M, Fulanovič L, Bradeško A, Drnovšek S, Malič B. Specific Heat Capacity and Thermal Conductivity of the Electrocaloric (1–x) Pb (Mg1/3Nb2/3) O3–xPbTiO3 Ceramics Between Room Temperature and 300oC. Inf Midem 2015;45:260–5.